5-2019

Numerical investigation of coalescence-induced self-propelled behavior of droplets on non-wetting surfaces and wedged surfaces.

Yan Chen
University of Louisville

Recommended Citation

Chen, Yan, "Numerical investigation of coalescence-induced self-propelled behavior of droplets on non-wetting surfaces and wedged surfaces." (2019). *Electronic Theses and Dissertations.* Paper 3244.
https://doi.org/10.18297/etd/3244

NUMERICAL INVESTIGATION OF COALESCENCE-INDUCED SELF-PROPELLED BEHAVIOR OF DROPLETS ON NON-WETTING SURFACES AND WEDGED SURFACES

By

Yan Chen
B.S., North China University of Water Conservancy and Electric Power, 2009
M.S., University of Louisville, 2011

A Dissertation
Submitted to the Faculty of the
J.B. Speed School of Engineering of University of Louisville
in Partial Fulfillment of Requirements
for the Degree of

Doctor of Philosophy
in Mechanical Engineering

Department of Mechanical Engineering
University of Louisville
Louisville, Kentucky

May 2019

NUMERICAL INVESTIGATION OF COALESCENCE-INDUCED SELF-PROPELLED BEHAVIOR OF DROPLETS ON NON-WETTING SURFACES AND WEDGED SURFACES

By

Yan Chen
B.S., North China University of Water Conservancy and Electric Power, 2009
M.S., University of Louisville, 2011

A Dissertation Approved on

September 17, 2018

by the following Dissertation Committee:

Dr. Yongsheng Lian
Dissertation Director

Dr. Ellen Brehob
Mechanical Engineering

Dr. Geoffrey Cobourn
Mechanical Engineering

Dr. Eric Berson
Chemical Engineering

ACKNOWLEGDMENTS

I would like to express my sincere gratitude to my advisor, Dr. Yongsheng Lian. Thank you for his academic guidance, support and encouragement towards the completion of my dissertation. I am grateful for his patience in leading me into a new area of multiphase flow simulation.

Thank you to Dr. Ellen Brehob, Dr. Geoffrey Cobourn and Dr. Eric Berson, for serving as my committee members.

Thank you to my former and current lab members. They are always warming, supportive, and encouraging.

Thank you to my family, for their love and support.

ABSTRACT

NUMERICAL INVESTIGATION OF COALESCENCE-INDUCED SELF-PROPPELLED BEHAVIOR OF DROPLETS ON NON-WETTING SURFACES AND WEDGED SURFACES

Yan Chen

September 17, 2018

When small drops coalesce on a superhydrophobic surface, the merged drop can jump away from the surface due to the surface energy released during the coalescence. This self-propelled behavior has been observed on various superhydrophobic surfaces and has potential applications in areas related to the heat and mass transfer, such as heat exchangers, anti-icing and anti-frost devices, thermal management and water harvesting. The jumping velocity model was obtained based on published experimental data and the balance of various energy terms described in previous studies. However, the self-propelled mechanism is still not fully understood.

In this study, the self-propelled droplet phenomenon upon droplet coalescence was numerically studied to understand the mechanism. A multiphase flow solver was used to solve the three-dimensional Navier-Stokes equations. The liquid-air interface was captured using the moment of fluid (MOF) along with a direction splitting method applied to advect the interface. An approximate projection method was used to decouple the calculation of velocity and pressure. Both static and dynamic contact angle models were used to represent the surface wettability.

The droplet jumping process was accurately captured by the multiphase flow solver. Both simulated droplet deformation and the vertical axis length matched the experimental results. Two cases with and without contact substrate were compared to investigate the jumping mechanism. With contact substrate, the droplet had double the time of acceleration in the upward direction. A high-pressure area appeared at the bottom of merged droplet and extended the acceleration. During the detachment the merged droplet with contact substrate also had a smaller surface area which indicates that more surface energy was converted into kinetic energy. The effects of droplet size, surface tension, and droplet density were studied. The jumping speed generally obeyed the capillary-inertial scaling law. The effect of approaching speed was also investigated. With lower approaching speed, the surface tension dominates while with higher approaching speed, the inertia force dominates the jumping process.

The effect of substrate curvature was studied, and the numerical results revealed that droplet peripheries were formed on the symmetric sides of the wedge. The peripheries forced the droplet transferring more surface energy into kinetic energy in the upward direction. The jumping velocity increased by increasing the surface curvature. The droplet size was studied on the wedged surface and it obeyed the capillary-inertial scaling law. Our study also showed that with a lower contact angle, the droplet jumping velocity decreased. And the droplet was unable to jump away from substrate if the contact angle was below certain value.

TABLE OF CONTENTS

LIST OF TABLES

LIST OF FIGURES

CHAPTER 1. INTRODUCTION

1.1 Coalescence Induced Jumping Behavior

Dropwise condensation plays an important role in engineering applications, such as heat exchangers (Reay et al., 2013), anti-icing and anti-frost devices (Boreyko et al., 2016; Zhang et al., 2013; Zhang et al., 2012), thermal management (Boreyko et al., 2013a; Dietz et al., 2010) and water harvesting (Kim et al., 2017; Lee et al., 2012). Because dropwise condensation occurs on a surface not completely wetted by the condensate, it is typically an order of magnitude more effective than filmwise condensation in phase-change heat transfer (Lienhard, 2013; Rose, 2002). In conventional dropwise condensation, drops must be removed by external forces to maintain high heat transfer efficiency. The most common approach to remove drops is gravitational removal, but this approach depends on the surface orientation. In addition, gravity can only affect drop size comparable to the capillary length (Rose et al., 1973).

Studies have shown that drops can self-propel and jump away from surfaces upon drop coalescence (Boreyko et al., 2009; Liu et al., 2014b; Miljkovic et al., 2012a; Nam et al., 2013; Zhang et al., 2015). The self-propelled capability has drawn enormous attentions (Boreyko et al., 2013b; Enright et al., 2013; Miljkovic et al., 2012a; Miljkovic et al., 2012b; Shi et al., 2015; Torresin et al., 2013) because it can automatically remove drops from the condensation surface, therefore, enhance heat transfer rate. During condensation, vapor experiences phase change to become liquid droplets.(McNaught et al., 1997) As the drops grow in size, adjacent drops contact each other and coalesce. The coalesced drop then spontaneously jumps away from the surface (Boreyko et al., 2009) or change from Wenzel state to Cassie state (Wang et al., 2011) when excess surface energy is released. Boreyko et al. also reported a self-propelled jumping motion of condensate drops on a super-hydrophobic surface and suggested that self-propelled jumping motion results due to the release of surface energy upon drop coalescence (Boreyko et al., 2009).

1.1.1 Energy Conversion

However, there is no agreement over how much excess surface energy can be converted to kinetic energy. Nam et al. (2013) found through numerical simulation that approximately half of the excess surface energy is converted into kinetic energy before the drop detaches from a superhydrophobic surface. Using Lattice Boltzmann simulation, Peng et al. (2013) claimed that about 25% of the energy released due to droplet coalescence can be converted into effective kinetic energy. However, Enright et al. showed that only 6% of the excess surface energy is convertible into translational kinetic energy (Enright et al., 2014). Through detailed measurements coupled with numerical simulations, they clarified the importance of internal fluid dynamics during the jumping droplet coalescence process.

1.1.1.1 Energy terms

During the coalescence process, energy is converted from one type to another among surface energy, kinetic energy, potential energy and viscous dissipation energy. The surface energy of a stationary droplet on a hydrophobic surface can be written as

$$E_s = \sigma_{lv} A_{lv} + \sigma_{ls} A_{ls} + \sigma_{sv} A_{sv} \tag{1}$$

where A is the interfacial area, σ is the surface tension and the subscripts s, l, and v denote the solid, liquid, and vapor, respectively.

During the coalescence, the kinetic energy of the merged droplet could be defined by

$$E_k = \frac{1}{2} \rho V (u^2 + v^2 + w^2) \tag{2}$$

where ρ is the liquid density, V is the droplet volume and u, v and w are velocities at x, y and z directions, respectively. The potential energy is given by

$$E_p = \rho V g z \tag{3}$$

where g is the gravitational acceleration and z is the altitude of the droplet.

The viscous dissipation energy for the droplet can be estimated as

$$E_{vis} = \int_0^t \left(\int_V \Phi dV \right) dt \tag{4}$$

where Φ is the dissipation function defined as

$$\Phi = \mu \left(2 \left((\frac{\partial u}{\partial x})^2 + (\frac{\partial v}{\partial y})^2 + (\frac{\partial w}{\partial z})^2 \right) + (\frac{\partial u}{\partial y} + \frac{\partial v}{\partial x})^2 + (\frac{\partial u}{\partial z} + \frac{\partial w}{\partial x})^2 + (\frac{\partial v}{\partial z} + \frac{\partial w}{\partial y})^2 \right) \tag{5}$$

where μ is the viscosity of the liquid, t is the time.

The changes in the surface energy ΔE_s, kinetic energy ΔE_k, potential energy ΔE_p, viscous dissipations ΔE_v, and total energy ΔE_t from the initial state denoted with subscript 0 are calculated as follows:

$$\Delta E_s = \sigma_{lv}\Delta A_{lv} + \sigma_{ls}\Delta A_{ls} + \sigma_{sv}\Delta A_{sv} \tag{6}$$

$$\Delta E_k = \int_V \frac{1}{2}\rho_l[(u^2+v^2+w^2)-(u_0^2+v_0^2+w_0^2)]dV \tag{7}$$

$$\Delta E_p = \rho_l V g(z-z_0) \tag{8}$$

$$\Delta E_v = \int_0^t \int_V (\Phi - \Phi_0)dVdt \tag{9}$$

$$\Delta E_t = \Delta E_s + \Delta E_k + \Delta E_p + \Delta E_v \tag{10}$$

1.1.2 Droplet Jumping Velocity Model

Extensive research (Boreyko et al., 2009; Liu et al., 2014a, b; Shi et al., 2015; Wang et al., 2011) has been conducted to investigate the jumping velocity of drop upon coalescence. Liu et al. (2014b) investigated the coalescence of identical water drops with a radius ranging from 20 to 500 μm on Leidenfrost surfaces with a contact angle of 180˚. They found the jumping velocity of the coalesced drop to be around 0.2 when scaled by the capillary–inertial velocity and the jumping velocity appears to be independent of the approaching velocity prior to coalescence if the approaching velocity is less than capillary-inertial velocity. Later, Liu et al. (2014a) conducted numerical simulations to explain the jumping mechanism. They found that the out of plane jumping results from the non-wetting substrate interfering with the oscillation of the merged drop. They claimed that when the liquid bridge between the droplets expands and reaches the substrate, the substrate counteracts the impingement of the drop and forces the downward-moving mass to the opposite direction. The vertical impulse from the substrate was predicted by the concept of elastic rebound from drop impact on the non-wetting substrate (Liu et al., 2014a).

In another study, Boreyko et al. (2009) observed that the coalescence-induced velocity at first increases and then decreases with the droplet size. This observation was later verified by a theoretical model of Wang et al. (2011), who claimed that the self-propelled behavior can only occur when the surface energy dominates the viscous dissipation rate and the gravitational potential energy. Recently, Shi et al. (2015) discovered that not only the radius of the droplet plays an important role in the self-propelled behavior, but the number of the droplets is also an important factor. More droplets could release more surface energy and therefore, the jumping height increases with the increase in droplet number.

1.1.2.1 Dimensionless analysis

To investigate the relationship between jumping velocity and other physical quantities, the dimensional analysis is conducted here for jumping velocity. The jumping velocity could be represented as a function of fluid density, surface tension, gravity, radius and viscosity.

$$w_j = f(\rho_l, \sigma, g, r_0, \mu) \tag{11}$$

The basic dimensions of variables are as follows

$$w_j \doteq LT^{-1} \quad \rho_l \doteq ML^{-3} \quad \sigma \doteq MT^{-2} \quad g \doteq MT^{-2} \quad r_0 \doteq L \quad \mu \doteq ML^{-1}T^{-1}$$

The repeating variables ρ, σ and r_0

$$\Pi = w_j \rho_l^a \sigma^b r_0^c \tag{12}$$

$$\Pi = \frac{w_j}{\sqrt{\frac{\sigma}{\rho_l r_0}}} \tag{13}$$

Therefore, the velocity scales with $\sqrt{\frac{\sigma}{\rho r_0}}$ and it is called capillary-inertial scaling law (Boreyko et al., 2009; Liu et al., 2014a).

$$w_j \sim u_{ci} = \sqrt{\frac{\sigma}{\rho r_0}} \tag{14}$$

Bond number is a dimensionless number measuring the ratio of surface tension forces to body forces, defined as

$$Bo = \frac{\Delta \rho g D_0^2}{\sigma_{lv}} \tag{15}$$

where $\Delta\rho$ is the difference in density of the two phases and D_0 is the drop diameter. The Ohnesorge number (Oh) is a dimensionless number that relates the viscous forces to inertial and surface tension forces , defined as

$$Oh = \frac{\mu}{\sqrt{\rho\sigma D_0}} \tag{16}$$

$Bo \ll 1$ and $Oh \ll 1$ during the process of small water drop coalescence, hence, the gravity and viscous effect only played a secondary role.

1.1.2.2 Theoretical jumping velocity model

Different models have been used to analyze the jumping velocity.(Enright et al., 2013; Liu et al., 2014b; Nam et al., 2013) The theoretical jumping velocity can be obtained when supposing all excessive surface energy are transferred into kinetic energy in jumping direction and the empirical model was obtained based on the experimental data (Enright et al., 2013; Liu et al., 2014b; Nam et al., 2013).

The release of excessive surface energy can be explained using a simple model shown in Figure 1. Here we consider two identical droplets of a radius of r_0. When they coalesce to form one larger droplet, the equivalent radius becomes

$$r = 2^{1/3} r_0 \tag{17}$$

and the merged drop has a mass of

$$m = \frac{8}{3}\rho_l \pi r_0^3 \tag{18}$$

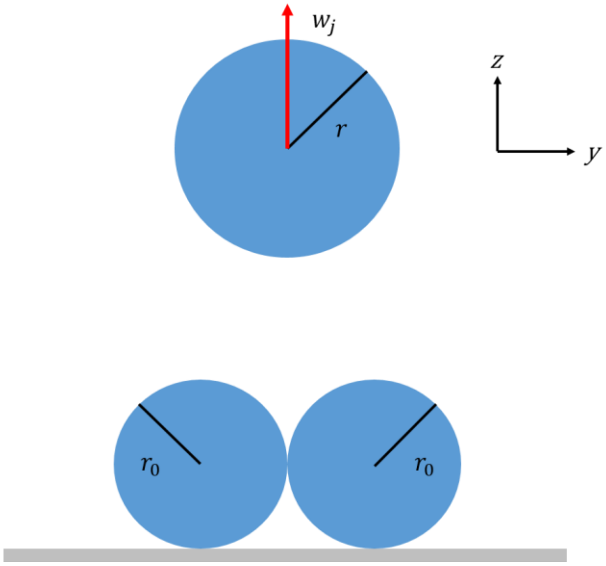

Figure 1 Schematic of the drop coalescence process on a non-wetting substrate.

The overall surface area is reduced upon coalescence, the released surface energy is defined as:

$$\Delta E_s = 4\sigma\pi r_0^2(2-2^{\frac{2}{3}}) \tag{19}$$

If the released surface energy is entirely changed into jumping kinetic energy, the maximum of the jumping velocity magnitude could be obtained.

$$\Delta E_s = \frac{1}{2} m w_{j,\max}^2 \tag{20}$$

$$4\sigma\pi r_0^2(2-2^{\frac{2}{3}}) = \frac{1}{2}\cdot\frac{8}{3}\rho_L \pi r_0^3 \cdot w_{j,\max}^2 \tag{21}$$

$$\sigma(2-2^{\frac{2}{3}}) = \frac{1}{3}\rho_L r_0 w_{j,\max}^2 \tag{22}$$

$$w_{j,\max} = \sqrt{3(2-2^{\frac{2}{3}})}\sqrt{\frac{\sigma}{\rho_L r_0}} \approx 1.11\sqrt{\frac{\sigma}{\rho_L r_0}} \tag{23}$$

Therefore, the limitations of the capillary–inertial scaling law can be understood from the energetic point of view above and the vertical jumping velocity (w_j) of merged identical drops is proportional to the capillary-inertial velocity (u_{ci}).

The corresponding characteristic time scale is

$$\tau_{ci} = \frac{r_0}{u_{ci}} = \sqrt{\frac{\rho r_0^3}{\sigma}} \tag{24}$$

1.1.2.3 Empirical jumping velocity models

Empirical models (Enright et al., 2014; Liu et al., 2014b) were obtained from experiments (Boreyko et al., 2009; Enright et al., 2014; Liu et al., 2014b). Liu et al. studied the coalescence-induced jumping on a Leidenfrost substrate (Liu, Ghigliotti et al. 2014). In the experiment, the contact angle is considered to be 180°. The droplet radius is in the range of $20 \sim 500$ μm. The jumping velocity upon drop coalescence is measured over a range of average initial radii. Their experiment indicated that the jumping velocity is independent of the relative approaching velocity. Based on their experiments, they suggested the following relationship between the jumping velocity and the capillary-inertial velocity

$$w_j = 0.2u_{ci} \tag{25}$$

And the experimental data and the estimation model are plotted in Figure 2.

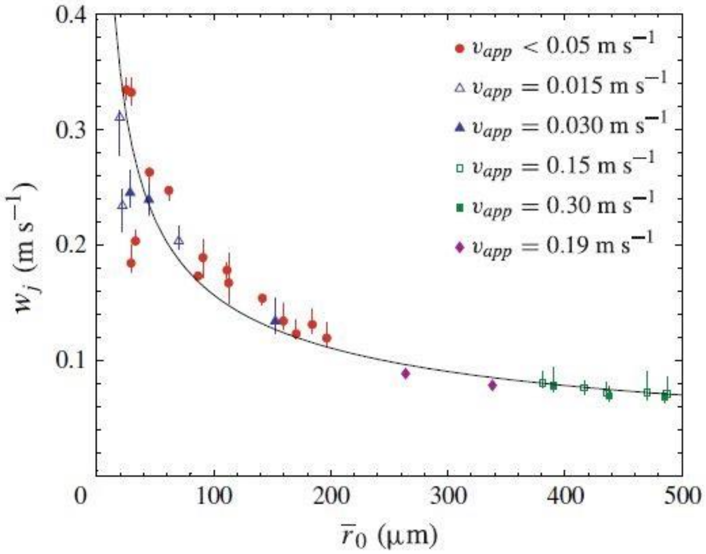

Figure 2 The droplet jumping velocity vs. droplet size (Liu et al., 2014b)

Enright et al. experimentally studied the jumping velocity of the coalesced droplet on superhydrophobic surface (Enright et al., 2014). The (CNT)-based superhydrophobic surfaces (Enright et al., 2014) with a structure spacing length scale of l ~ 100 nm and CuO nanostructures were used in Enright's studies (Enright et al., 2013; Enright et al., 2014). The droplet radius is in the range of 10~50 μm. The advancing contact angle of CNT surface is $\theta_a^{app} = 170.2°$ ($\cos\theta_a^{app} = \cos(170.2°) = -0.985 \approx -1$) and the CuO surface has an advancing contact angle of $\theta_a^{app} = 169.2°$. They fitted both their experimental data and Boreyko et al's data (Figure 3) into their jumping velocity model(Enright et al., 2014). They proposed the following model to predict jumping velocity

$$w_j = Du_{ci} = D\sqrt{\frac{\sigma}{\rho_L r_0}} \tag{26}$$

where parameter D is a function of the Ohnesorge number, Oh

$$D = 3.4026Oh^2 - 1.5285Oh + 0.2831 \tag{27}$$

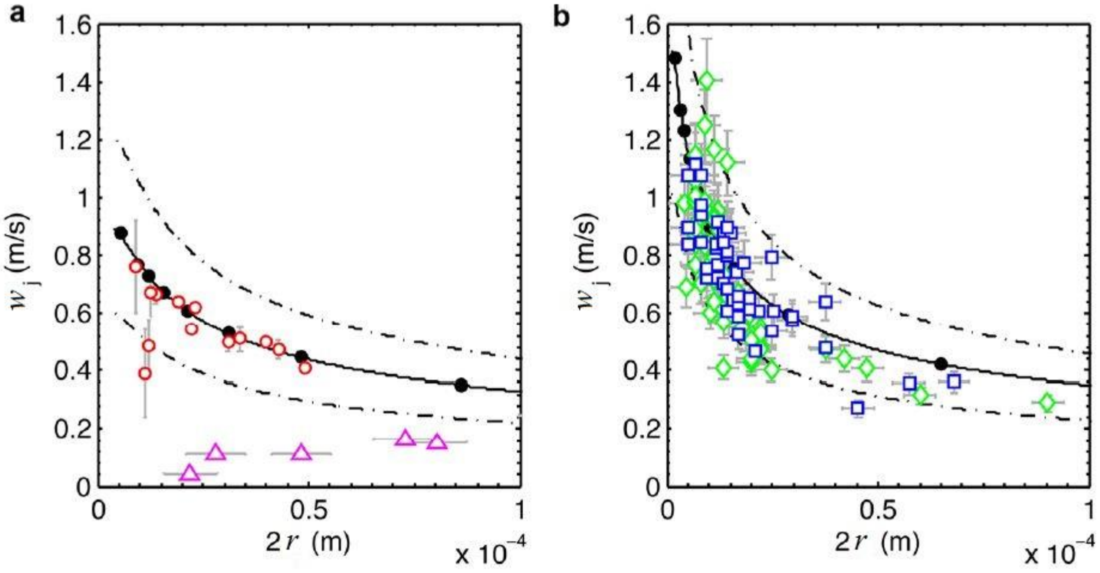

Figure 3 The droplet jumping speed vs. droplet size on CNT (Enright et al., 2014) and CuO (Enright et al., 2013) nanostructured surfaces. The open circles are the data at the temperature of 20 ℃ and the open triangles at the temperature of 5 ℃ on the CNT surface. The squares and diamonds are the data at the temperature of 20℃ from the CNT and CuO surfaces, respectively.

The energy conversion efficiency of the process is defined as follows

$$\eta_j = \frac{E_j}{\Delta E_s} = \frac{0.5mw_j^2}{\Delta E_s} \tag{28}$$

When viscous dissipation is neglected, and the droplet shape is perfect round, η_j is 1.

Using Liu et al.'s jumping velocity model (Liu et al., 2014b) (Eq (25)), the efficiency is about 3%. Based on Enright's model in Eq (26), the efficiency should be calculated using the following equation

$$\eta_i = \frac{D^2}{1.24} \tag{29}$$

The efficiency reduces from ~6% at $D \approx 0.28$ ($Oh \rightarrow 0$) down to ~1.8% at $D \approx 0.15$ ($Oh = 0.12$) in their experiment.

1.1.3 Droplet Coalescence

The jumping motion is due to the non-wetting substrate interfering with the oscillation of the coalesced drop (Liu et al., 2014a). The droplet coalescence in the air is illustrated in Figure 4. Two initially distinct droplets of identical size are adjacent to each other. At the beginning of the coalescence, a liquid bridge is formed to merge the two separate droplets. The liquid bridge expands quickly and pulls two droplets together due to surface tension. The two droplets finally merge into a larger droplet. After the early-stage bridging process (Baroudi et al., 2015; Eggers et al., 1999; Sprittles et al., 2012), the coalesced droplet oscillates for a few wavelengths until it relaxes into a stable spherical form.

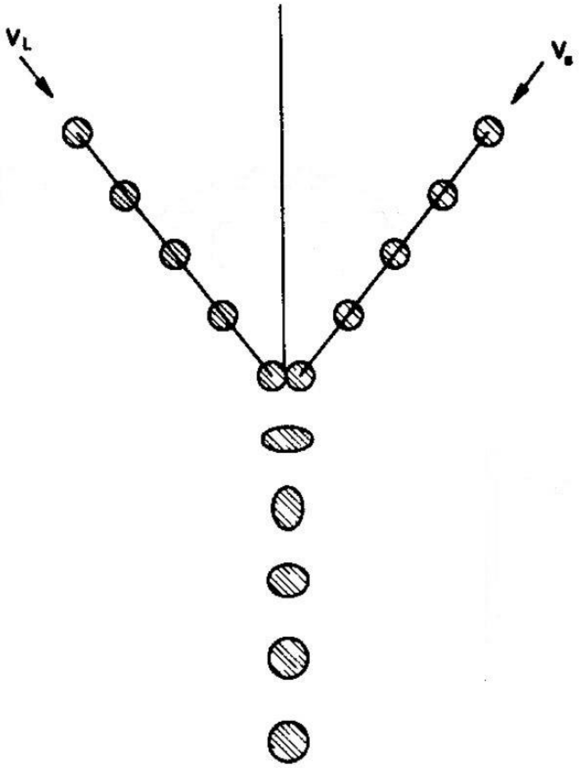

Figure 4 Binary droplet collision resulting stable coalescence and oscillation(Orme, 1997)

1.1.3.1 Droplets collision regimes

The dynamics of binary droplet collision exist in various spray processes, such as dense sprays, liquid–liquid extraction, emulsion polymerization, waste treatment, and hydrocarbon fermentation (Shah et al., 1972). The outcome of droplet collision, whether is coalescence or not, depends on the droplet properties and collision condition. Qian et al. divided the droplets collision outcomes into five regimes in their study (Qian et al., 1997), (I). coalescence after minor deformation, (II). bouncing, (III). coalescence after substantial deformation, (IV) coalescence followed by separation for near head-on collisions, and (V) coalescence followed by separation for off-center collisions. The water droplets exhibit three regimes for the collision outcome in atmospheric air (Figure 5) and more regimes in high-pressure condition.

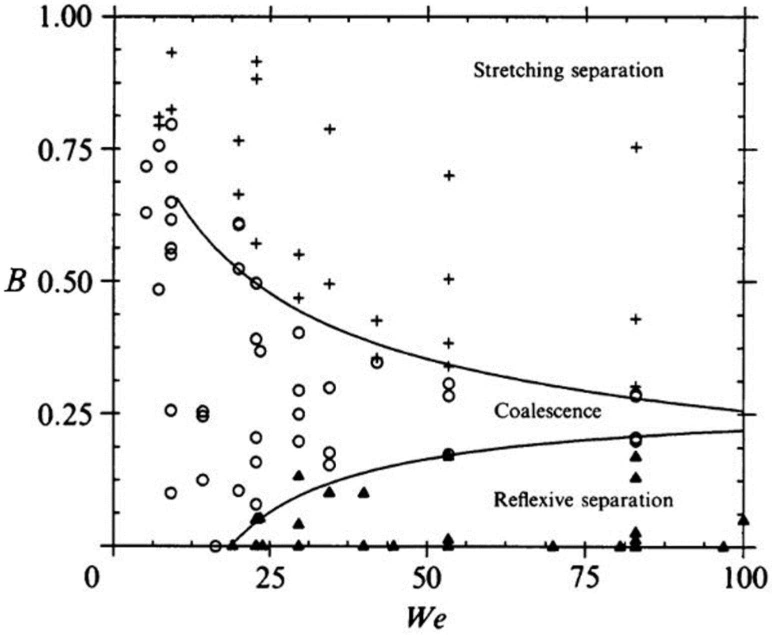

Figure 5 Schematic of collision regimes of water droplets in 1 atm. air (Ashgriz et al., 1990; Qian et al., 1997)

Those various regimes for collision outcome are depending on the pressure of atmospheric air, Weber number We and impact parameter *B* (Qian et al., 1997). The Weber number represents the ratio of the inertial force to the surface-tension force, defined as

$$We = \frac{4\rho U_0^2 D}{\sigma} \tag{30}$$

and the impact parameter is

$$B = \frac{b}{D} \tag{31}$$

where U_0, D and b are the droplet speed, droplet diameter and the distance of the droplets in the direction normal to the relative droplet velocity, as shown in Figure 6.

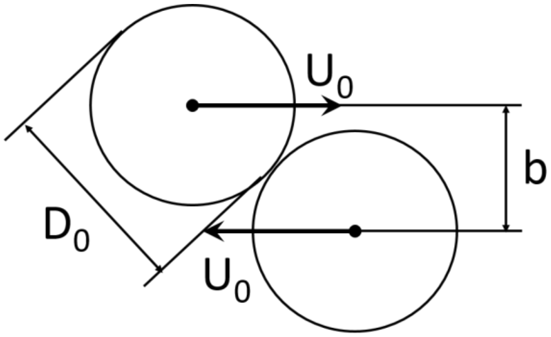

Figure 6 The kinetic and geometric parameters of the collision of two equalized drops.

1.1.3.2 Droplet oscillation

The oscillation could be considered as a large-amplitude two-lobed perturbation at spherical equilibrium and related to the oscillation of a single drop (Liu et al., 2014a). The droplet preserved top-down symmetry during the oscillation and the oscillation was eventually damped out by viscous force (Liu et al., 2014a; Zou et al., 2011).

Due to the importance of droplet oscillation, the theorectical oscillation frequency (Becker et al., 1991; Chandrasekhar, 2013; Rayleigh, 1879a) is presented here. The Rayleigh mode (Rayleigh, 1879a) decribes the deformation of the droplet shape by infinite series of surface spherical harmonics. And the frequency of the oscillation depends on the mode of oscillation, defined as:

$$f = \frac{1}{2\pi}\sqrt{\frac{\sigma n(n-1)(n+1)}{\rho r^3}} \tag{32}$$

where $n = 2$ for oscillation with elliptical shape, σ and ρ is the surface tension and density, respectively, and r is the merged droplet radius ($2^{1/3} r_0$).

$$f = \frac{\sqrt{3}}{2\pi}\sqrt{\frac{\sigma}{\rho r_0^3}} = \frac{\sqrt{3}}{2\pi\tau_{ci}} \tag{33}$$

And the corresponding period is $T = 2\pi / \sqrt{3}\tau_{ci}$.

1.2 Effect of Substrate Surface

The self-propelled phenomenon has been discovered on various surfaces. Lv et al.(Lv et al., 2013) discovered the remarkable out of plane continuous jumping relay of condensed droplet trigged by falling droplets on a lotus leaf. Wang et al.(Wang et al., 2015) showed that droplets of volume ranging from femtoliter to microliter could be self-removed from the legs of water striders due to the arrays of inclined tapered setae decorated by quasi-helical nanogrooves on legs. The water repellent capability of the lotus leaf and other natural surfaces has inspired numerous researches of the superhydrophobic patterned surface.(Bhushan et al., 2011; Burton et al., 2005; Gao et al., 2006; Giacomello et al., 2012; Wu et al., 2011) The micro-nano patterned surface shows very low adhesive force to water droplets.(Gao et al., 2006; Koch et al., 2009; Liu et al., 2014c) Liu et al.(Liu et al., 2014b) used a Leidenfrost surface to better approaching nonwetting surface for coalescence induced jumping study although it is despite difficult to maintain the Leidenfrost surface than patterned superhydrophobic surface. Therefore, the surface has a positive effect on the self-propelled behavior.(Cheng et al., 2016; Dietz et al., 2010) It is necessary to maintain the nonwetting surface to achieve the self-propelled behavior.

1.2.1 Wetting Fundamentals

1.2.1.1 Surface tension

The surface tension is a fundamental property of liquids. In a pure liquid, neighboring liquid molecules in the bulk pull each other equally in every direction, resulting in a net force of zero. However, the molecules exposed at the surface cannot balance the forces in all directions. They are pulled inward by the neighboring molecules creating a “tension”. As a result, some internal pressure is created, and the surface tension acquire the least surface area possible. The Gibbs free energy G of a system is the thermodynamic potential of a system with temperature *T*, pressure *p* and the particle number *N*. In equilibrium, this energy is per definition at a minimum. The Gibbs free energy of an area for fixed pressure and temperature is the determined by the surface tension (Butt et al., 2006)

$$\sigma = \left(\frac{\partial G}{\partial A} \right)_{T,\mathrm{p},\mathrm{N}} \tag{34}$$

where G is Gibbs free energy and A is the area.

The Young–Laplace Law describes the capillary pressure difference sustained across the interface between two static fluids caused by surface tension force. Surface tension pulls at this rectangle from all four sides, as shown in Figure 7. In the 1-direction surface tension acts with two nearly opposite forces of magnitude σdl_2, each forming a tiny angle of magnitude $\frac{1}{2} dl_1 / R_1$

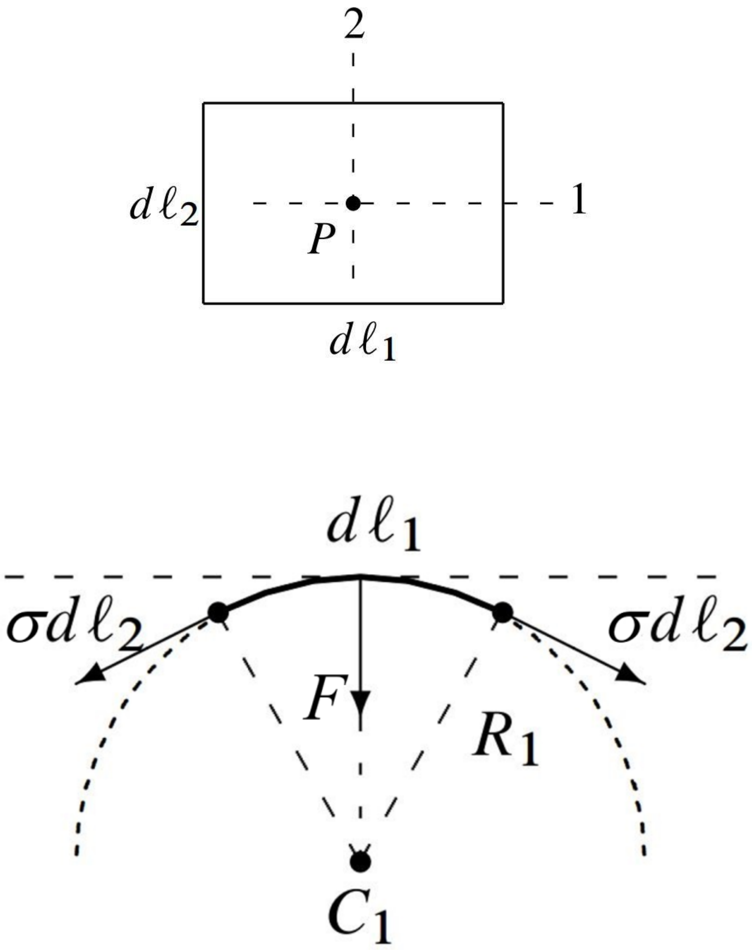

Figure 7 Surface tension force at the interface (Lautrup, 2011)

The Young–Laplace Law describes the capillary pressure difference sustained across the interface between two static fluids caused by surface tension force. Surface tension pulls at this rectangle from all four sides. In the 1-direction surface tension acts with two nearly opposite forces of magnitude αdl_2, each forming a tiny angle of magnitude $\frac{1}{2}dl_1 / R_1$.

Projecting the two forces on the normal, the total force in the direction of the center of curvature C_1 is

$$dF = 2\cdot\sigma dl_2 \cdot \frac{1}{2} dl_1 / R_1 = \sigma dA / \mathrm{R}_1 \tag{35}$$

where $dA = dl_1 \cdot dl_2$ and R_1 is the radius of curvature in 1-direciton. Divided by dA, the pressure difference at the surface is

$$\Delta p = \frac{\sigma}{R_1} \tag{36}$$

Adding the contribution from the 2-direction it is the Young–Laplace law (De Gennes et al., 2013) for the pressure discontinuity due to surface tension,

$$\vartriangle p = \sigma(\frac{1}{R_1} + \frac{1}{R_2}) \tag{37}$$

Δp is called Laplace pressure or capillary pressure if it is due to the wall tension. In spherical shapes ($R_1 = R_2 = R$), the Laplace pressure is simplified as

$$\Delta p = \frac{2\sigma}{R} \tag{38}$$

where R is the radius of curvature of the spherical shape.

1.2.1.2 Contact angle and hysteresis

The contact angle is used to specify the characteristic of a given solid-liquid system in a specific environment. In 1805, Thomas Young was the first to quantify wettability in form of an interfacial property called “contact angle” (Young, 1805). Essentially, the model is a two-dimensional force balance at the contact line of a droplet. The force balance relates the three principal interfacial energies: the liquid-vapor interfacial energy σ_{lv}, the solid-liquid interfacial energy σ_{sl}, and the vapor-solid interfacial energy σ_{sv}. The vertical force from σ_{lv} is balanced by the substrate and the horizontal forces have a relation to reaching the ideal balance:

$$\cos\theta_Y = \frac{\sigma_{SV} - \sigma_{SL}}{\sigma_{LV}} \tag{39}$$

where θ_Y is Young’s contact angle. The principles of hydrophilicity ($0° < \theta_Y < 90°$) and hydrophobicity ($90° < \theta_Y < 180°$) introduced earlier can be quantified using θ_Y illustrated in Figure 8.

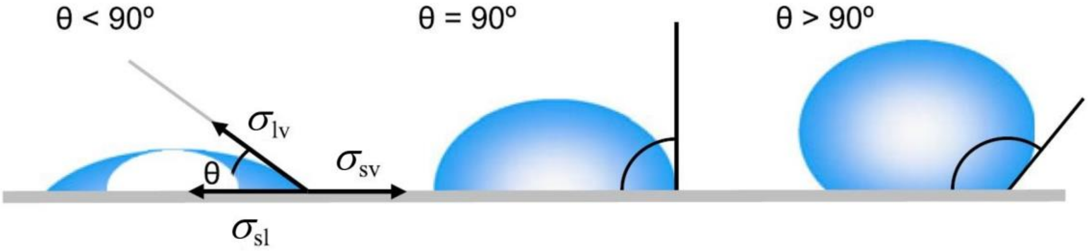

Figure 8 Illustration of contact angles formed by liquid drops on a smooth homogeneous solid surface (Yuan et al., 2013)

However, many metastable states of a droplet exist on a solid in practice, and the observed contact angles are usually not equal to θ_Y (Lam et al., 2002; Neumann et al., 1998). The phenomenon of wetting is just a static state. The measurement of a single static contact angle to characterize wetting behavior is not adequate. Different angles could be observed depending on how they are measured, how they are defined, or in the history of the contact angle formation(Yuan et al., 2013). In particular, the contact angle formed by expanding is referred to as the advancing contact angle θ_a and the one formed by contracting is receding contact angle θ_r , as shown in Figure 9 (De Gennes, 1985). The hysteresis is used to describe the relation of the immobile contact line (contact line is where the liquid contacting the surface) and contact angle, and is defined as the difference between the advancing contact angle and the receding contact angle for a contact line moving in opposite direction at the same velocity.

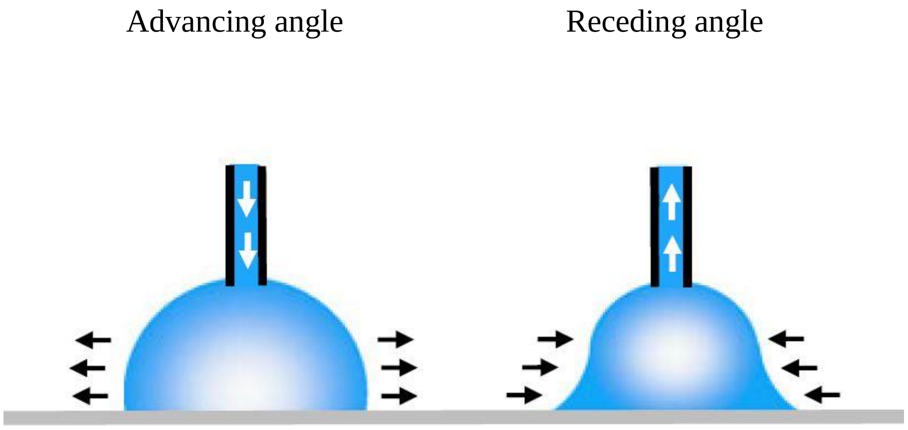

Figure 9 Advancing contact angle and receding contact angle (Yuan et al., 2013)

Figure 10 is a sketch that relates contact line to drop volume during the expansion and retraction of a drop on a solid surface. The initial radius of contact line and the initial contact angle are dependent on how it has been placed. At the beginning, the contact line is pinned, and the droplet does not change its radius from state 1 to 2 with the liquid injecting. When the contact angle exceeds the advancing contact angle at point 2 and the drop expands to state 3. From state 3 to state 4, the change of the contact angle could compensate the liquid drawing. At point 4, the drop contracts back since the contact angle is fallen below the receding angle.

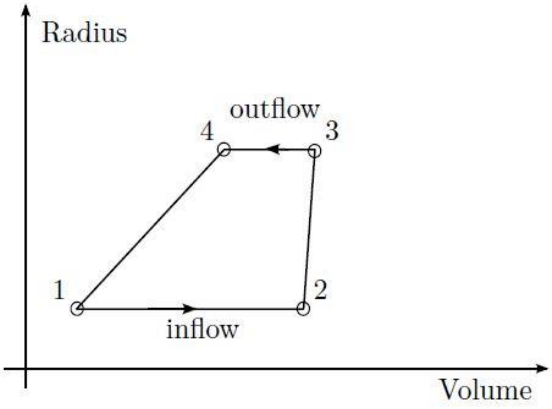

Figure 10 Sketch of a possible relation of the drop volume and the radius of contact line to describe the hysteresis(Linder, 2015)

The contact angle changes dynamically depending on the capillary number in advancing and receding phase, as shown in Figure 11 (Eral et al., 2013). The contact angle clearly depends on the contact line moving velocity even for cases with only a single contact line, while the static part of the hysteresis will be essentially invisible. The contact angle hysteresis (CAH) consists of two parts, the static hysteresis and the dynamic increase of the advancing contact angle or the dynamic decrease of the receding angle.

There is a jump in the contact angle at zero velocity. The dynamic component of the hysteresis is caused by the interplay of the liquid motion with the solid surface. For a slow-moving drop on a rough surface the static hysteresis will dominate, but for high velocities or low static CAH surfaces (especially on liquids or liquid-soaked solids) the dynamic hysteresis becomes extremely important.

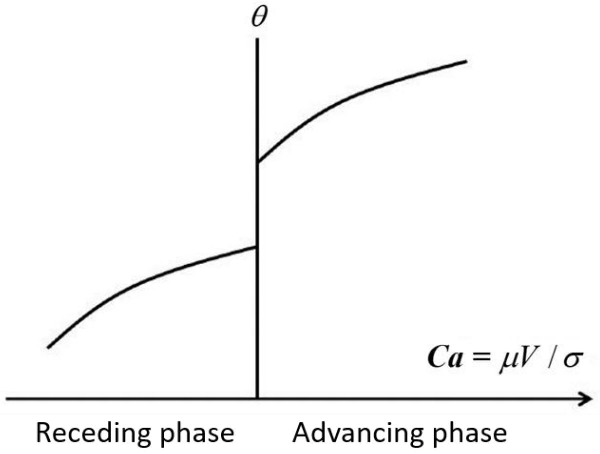

Figure 11 Schematic of contact angle hysteresis (Eral et al., 2013)

1.2.2 Effect of Surface Curvature

The curved surface was found to have a positive effect on the liquid bouncing performance (Hao et al., 2015). Wu et al. (2011) found that the contact angle of a bending patterned surface increased from 150° to 160° and the adhesion force decreased significantly with a smaller curvature. Hao et al. (2015) investigated a water droplet bouncing capability with the thin oil film on three different surfaces. The bouncing phenomenon happened only on a spherical surface but not on the other two surfaces with different arrays. Liu et al. (2015) found the contact time of droplet bouncing on the curved surface was 40% shorter than that on the equivalent flat surface (De Ruiter et al., 2015; Kolinski et al., 2014; Richard et al., 2002). A faster asymmetric bouncing phenomenon due to curved surface is being observed in both experimental and simulation based study (Liu et al., 2015). Zhang et al. (Zhang et al., 2015) studied self-propelled behavior on fiber-based coalescers and claimed that the curvature of fiber played a critical role in the self-bouncing capability of the droplets upon coalescence. The self-bouncing process upon drop coalescence happened on the fiber with contact angles of $\theta_A / \theta_R = 120° / 110°$ (where θ_A and θ_R are the advancing and receding contact angles, respectively) while it didn’t happen on the flat surface with same contact angles. The less liquid-solid contact area of the fiber was believed to be the reason (Zhang et al., 2015). It attained more upward momentum by reducing the drop-substrate adhesion. The early intervention to the coalescence effectively harnessed the released energy toward useful translational motion.

1.3 Objectives and Organization

It is still not quite clear how the surface energy is converted to kinetic energy, especially the effective kinetic energy in the jumping direction. The objective of this dissertation is to numerically investigate the jumping mechanism of the coalescence induced self-propelled behavior and the effects of liquid properties and substrate characteristics on the behavior.

Chapter 2 presents the numerical methods of the multiphase flow solver. The Navier-Stokes equations were solved using an approximate projection method. The moment of fluid method was used to reconstruct interfaces between different phases. A dynamic contact angle model was used to define the boundary condition at the contact line.

Chapter 3 presents the numerical study of droplet (with a radius of $380\ \mu\text{m}$) coalescence on a nonwetting surface. The numerical method is validated by comparing with available experimental data. The grid sensitivity analysis is conducted to guarantee the accuracy and efficiency.

Chapter 4 investigates the jumping mechanism of the coalescence induced jumping behavior. The results are compared between two cases with and without contact substrate. The development of the jumping motion is investigated by examining the flow field in the droplet and the momentum history. The energy history is also studied for the purpose of analyzing energy conversation. The effects of surface tension, density and size of the droplet are investigated to validate the capillary-inertial scaling law. The effect of the approaching velocity is also studied.

Chapter 5 investigates the effects of surface tension, density and size of the droplet on the jumping behavior. The jumping speed is calculated to validate the capillary scaling law. The effect of the approaching velocity is also studied.

Chapter 6 studies the coalescence induced jumping behavior on the wedged surfaces. The droplet motions on the convex surface and fiber are simulated and the numerical method is validated by comparing them with experimental data. The curvature effect of the wedged surface is investigated. The capillary-inertial scaling law is validated on the wedged surface. The effect of the surface adhesion on the wedged surface is investigated.

Chapter 7 concludes the dissertation.

CHAPTER 2. NUMERICAL METHODS

The numerical method is based on a welled validated multiphase flow solver that solves the three-dimensional Navier-Stokes equations. The liquid-air interface is captured using the Moment of Fluid (MOF) method (Dyadechko et al., 2005; Jemison et al., 2013a) along with a directional splitting method (Li et al., 2015) applied to advect the interface. And an approximate projection method (Jemison et al., 2013a, b; Li et al., 2015) is used to decouple the calculation of velocity and pressure.

2.1 Governing Equations

The immiscible two-phase flows are modeled with incompressible Navier-Stokes equations.

$$\nabla \cdot \boldsymbol{u} = 0 \tag{40}$$

$$\frac{\partial \boldsymbol{u}}{\partial t} + \boldsymbol{u} \cdot \nabla \boldsymbol{u} = -\frac{\nabla p_m}{\rho_m} + \frac{\nabla \cdot (2\mu_m D)}{\rho_m} + \boldsymbol{g} \qquad \text{if } \phi_m(x,t) > 0 \tag{41}$$

where $\boldsymbol{u} = (u, v, w)$ is the velocity vector, t is the time, p is the pressure, $\boldsymbol{g}$ is the gravitational acceleration vector, D is the rate of deformation tensor,

$$D = \frac{\nabla \boldsymbol{u} + (\nabla \boldsymbol{u})^T}{2} \tag{42}$$

and ρ and μ are the combined density and viscosity for material m and are defined as follows,

$$\rho = \sum_{m=1}^{M} \rho_m H(\phi_m) \tag{43}$$

$$\mu = \sum_{m=1}^{M} \mu_m H(\phi_m) \tag{44}$$

where ρ_m and μ_m are the density and viscosity for material *m*, respectively, and where $H(\phi_m)$ is the Heaviside function defined as

$$H(\phi_m) = \begin{cases} 1 & \phi_m \geq 0 \\ 0 & \text{otherwise} \end{cases} \tag{45}$$

where ϕ_m is a level set function specifying distance to the interface for material *m* and satisfies

$$\phi_m(x,t) = \begin{cases} > 0 & \text{for material m} \\ \leq 0 & \text{otherwise} \end{cases} \tag{46}$$

and the transport of level set function is governed by

$$\frac{\partial \phi_m}{\partial t} + \boldsymbol{u} \cdot \nabla \phi_m = 0 \tag{47}$$

The stress at a material interface of material m_1 and material m_2 follows the jump condition which takes the effect of surface tension force.

$$((-p_{m_1} I + 2\mu_{m_1} D) - (-p_{m_2} I + 2\mu_{m_2} D)) \cdot \boldsymbol{n}_{m_1} = \sigma_{m_1,m_2} \kappa_{m_1} \boldsymbol{n}_{m_1} \tag{48}$$

where σ_{m_1,m_2} is the surface tension coefficient, $\boldsymbol{n}_{m1}$ is the normal pointing from material m_2 into m_1,

$$\boldsymbol{n}_{m1} = \frac{\nabla \phi_{m1}}{|\nabla \phi_{m1}|} \tag{49}$$

and κ_{m_1} is the curvature defined as

$$\kappa_{m_1} = \nabla \cdot \frac{\nabla \phi_{m_1}}{\left|\nabla \phi_{m_1}\right|} \tag{50}$$

For two material case,

$$\gamma_1 = \sigma_{12} \tag{51}$$

For three material case,

$$\gamma_1 = \frac{\sigma_{12} + \sigma_{13} - \sigma_{23}}{2} \tag{52}$$

$$\gamma_2 = \frac{\sigma_{12} + \sigma_{23} - \sigma_{13}}{2} \tag{53}$$

$$\gamma_3 = \frac{\sigma_{13} + \sigma_{23} - \sigma_{12}}{2} \tag{54}$$

2.2 Overview of the Method

The numerical method here is based on an approximate projection method. The moment-of-fluid reconstruction technique is applied to simulate the surface tension effects. The key steps of the MOF algorithm are described as follows:

1. Reconstruction of the interface: The new interface is reconstructed by tracking back position in the previous time step. The volume fraction F_m^n, and centroid $\boldsymbol{x}_m^n$ could be calculated for material m.

2. Advection: In order to proceed at time step $t = t^{n+1}$, the information of flow field from time step $t = t^n$ is given in each computational cell Ω. The level set function, ϕ_m^n, the volume fraction, F_m^n, and the location of the centroid $\boldsymbol{x}_m^n$ are given for each cell. These interface quantities are advected and the cell-centered advection velocity $\boldsymbol{u}^{advect}$ is calculated using a directionally split algorithm (Jemison et al., 2013a). The new values are denoted by $\phi_m^{n+1}, F_m^{n+1}, x_m^{n+1}$ and $\boldsymbol{u}^{advect}$.

3. Evaluation of the effect of viscosity, gravity and surface tension: The viscosity effect is calculated using an explicit sub-cycling algorithm (Li et al., 2015). The ghost fluid method is applied for spatial discretization of the surface tension force (Kang et al., 2000). The new temporary cell centered velocity, $\boldsymbol{u}*$, is given.

$$\boldsymbol{u}* = \boldsymbol{u}^{advect} + \Delta t \frac{1}{\rho}(\nabla \cdot (2\mu D) + \rho g - \sum_{m=1}^{M} \gamma_m \kappa_m \nabla H(\phi_m)) \tag{55}$$

4. Pressure projection: The remaining parts of momentum equation are solved using a projection method.

$$\nabla \cdot \frac{\nabla p}{\rho} = \frac{1}{\Delta t} \nabla \cdot \boldsymbol{u}* \tag{56}$$

$$\boldsymbol{u}^{n+1} = \boldsymbol{u}^* - \Delta t \frac{\nabla p}{\rho} \tag{57}$$

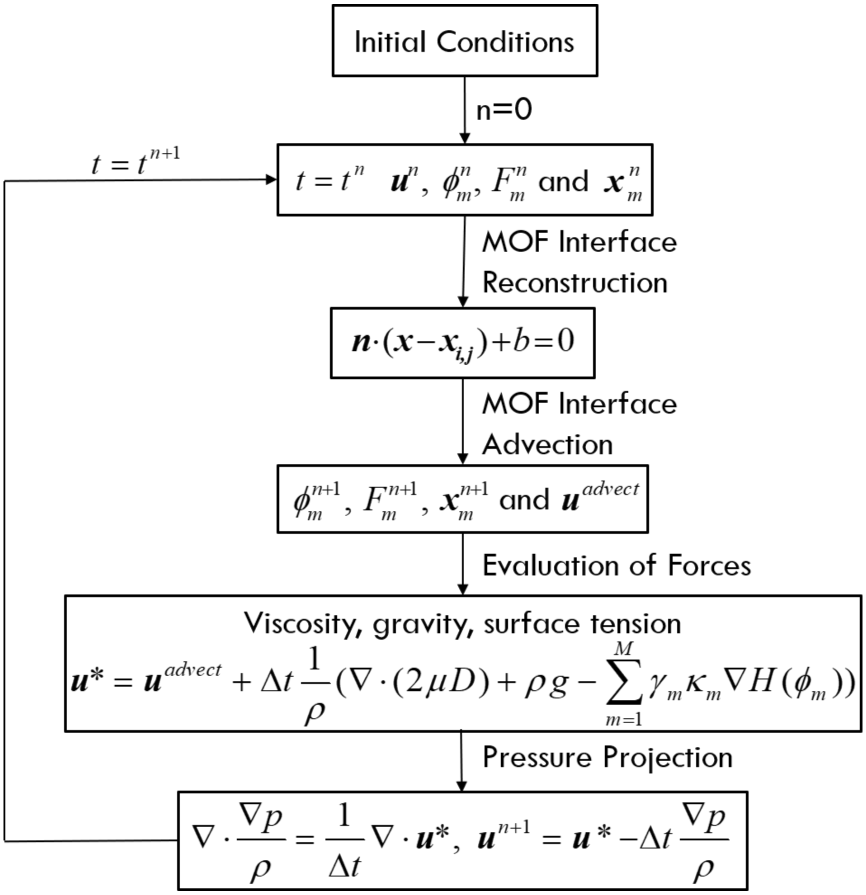

Figure 12 Process diagram of MOF method

2.3 MOF Interface Reconstruction

In this study, a moment-of-fluid method (Ahn et al., 2007, 2009; Dyadechko et al., 2005, 2008; Jemison et al., 2013b) is used to construct the interfaces between different phases. The MOF method can be considered as volume of fluid (VOF) methods generally, but only uses information from the computational cell under consideration. In addition to the volume fraction function used in the VOF method, the MOF method includes the material centroid information for interface reconstruction. In the local interface reconstruction, a slope and an intercept are produced by using information from volume fraction function and reference centroid. The MOF method was found more accurate than VOF methods, level set methods or CLSVOF methods (Jemison et al., 2013b; Wang et al., 2012).

For a computational cell Ω, the volume fraction and centroid of the material m are

$$F_m = \frac{\Omega_m}{\Omega} = \frac{1}{|\Omega|} \int_\Omega H(\phi_m(\boldsymbol{x}))d\boldsymbol{x} \tag{58}$$

$$\boldsymbol{x}_m = \frac{\int_\Omega H(\phi_m(\boldsymbol{x}))\boldsymbol{x}d\boldsymbol{x}}{\int_\Omega H(\phi_m(\boldsymbol{x}))d\boldsymbol{x}} \tag{59}$$

The interface in each cell is approximated by a plane in 3D or a line in 2D. The reconstruction procedure of interface is called piecewise linear interface calculation (PLIC). The interface line in 2D, as shown in Figure 13, can be represented by

$$\boldsymbol{n} \cdot (\boldsymbol{x} - \boldsymbol{x}_{\boldsymbol{i,j}}) + b = 0 \tag{60}$$

where $\boldsymbol{n}$ is the interface normal, $\boldsymbol{x}_{\boldsymbol{i,j}}$ is the computational cell center and b is the intercept. Analogously, the 3D interface plane can be obtained.

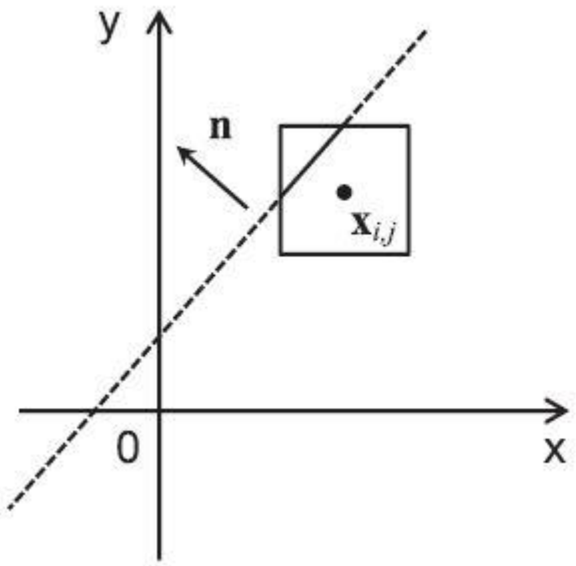

Figure 13 The interface can be represented by a straight line in 2D case, the square is a computational cell and $\boldsymbol{x}_{i,j}$ is the coordinate of cell center

The interface normal and the intercept can be calculated by solving an optimization problem. In the optimization problem we require:

$$|F_{ref} - F_{act}| = 0 \tag{61}$$

$$E_{MOF} = \| \mathbf{x}^c_{ref} - \mathbf{x}^c_{act} \|^2 \tag{62}$$

where F_{ref} and x_{ref} are the reference volume fraction and reference centroid from either the initial condition or from previous time step. And $\boldsymbol{x}^c_{act}$ and F_{act} are actual centroid function and volume fraction from the reconstructed interface. Eq. (61) requires the material volume from the constructed interface to match the reference volume, a similar technique used in the volume of fluid (VOF) method. Eq. (62) requires the actual centroid from the reconstructed volume to be as close to the reference centroid as possible.

An example of MOF interface reconstruction is shown in Figure 14. The real distribution of material m (green area) within a cell of size $a \times a$ is given in left picture, where the solid curved line represents the interface of the semi-circle with radius of $0.5a$. The right picture is the actual cell with the dashed straight line representing the reconstructed interface. In the left picture, volume fraction is $F_{ref} = 0.125\pi a^2 / a^2$. The volume fraction defined by the reconstructed interface on the right picture satisfies $F_{act} = F_{ref} = 0.125\pi$. The actual centroid $\boldsymbol{x}_{act}^{c} = (1/2a, \pi/16a)$ is the closest approximation to $\boldsymbol{x}_{ref}^{c} = (1/2a, 2/(3\pi)a)$ by minimizing equation (62). The problem is numerically solved with Gauss-Newton algorithm. For the detailed steps refer to Li et al. (2015).

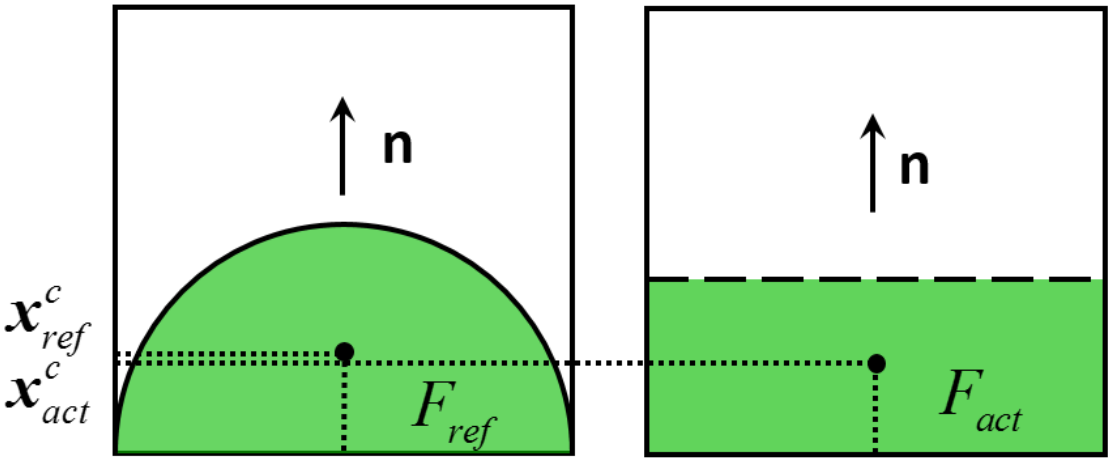

Figure 14 MOF interface reconstruction.

2.4 MOF Interface Advection

After constructing the interface, we advect the interface to the next time step. The direction splitting method (Jemison et al., 2013b; Strang, 1968) is used to integrate the interface position. As illustrated in Figure 15, a target computational cell occupying region Ω at time step t^{n+1} is traced backward in time to find its previous position Ω^{depart} at time step t^n , and the Ω^{depart} will advect to the target region Ω .

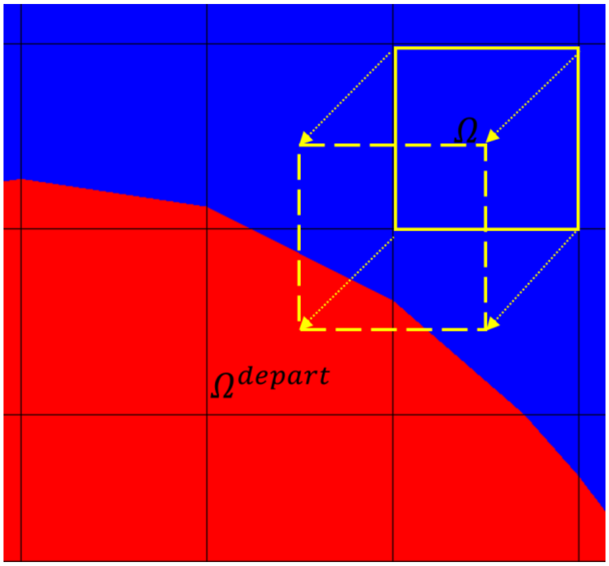

Figure 15 Backward projection for the directionally split method. The solid square on the top right represents the target region of the cell Ω ; the dashed square represents the departure region of the cell Ω^{depart} .

The interface integration process is illustrated only in the x direction here. The process is illustrated in a computational cell

$$\Omega_i = \{\boldsymbol{x} : x_{i-1/2} < x < x_{i+1/2}\} \tag{63}$$

As illustrated in Figure 15, Ω_i is traced backward in time to find its previous position Ω_i^{depart} (the departure region). The departure region can be written as follows:

$$\Omega_i^{depart} = \{x_{i-1/2} - u_{i-1/2}\Delta t < x < x_{i+1/2} - u_{i+1/2}\Delta t\} \tag{64}$$

where $u_{i-1/2}$ and $u_{i+1/2}$ are the horizontal velocities on the cell interface. The velocities are discretely divergence free. i.e. in 2D

$$\frac{u_{i+1/2,j}-u_{i-1/2,j}}{\Delta x}+\frac{v_{i,j+1/2}-v_{i,j-1/2}}{\Delta y}=0 \tag{65}$$

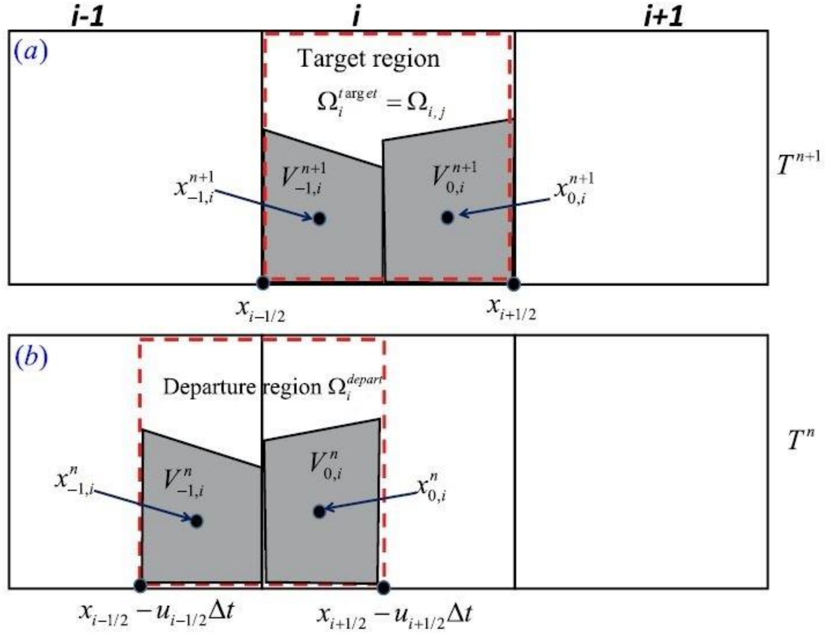

Figure 16 Backward projection for the directionally split method in x direction (Li et al., 2015). The dashed square in (a) represents the target region Ω_i; the shaded region in (a), $\Omega_{m,i}=V^{n+1}_{-1,i}\bigcup V^{n+1}_{0,i}$, is the material m, in the target region. The dashed square in (b) represents the departure region of cell i, Ω_i^{depart}; the shaded region in (b), $\Omega_{m,i}^{depart}=V^{n}_{-1,i}\bigcup V^{n}_{0,i}$, is the material m, in the departure region.

A linear mapping function T_i (Jemison et al., 2013a) is used to map between the two regions.

$$T_i:\Omega_i^{depart}\rightarrow\Omega_i \tag{66}$$

$$T_i: \quad x^T = \alpha x + \beta = \frac{\Delta x(x-(x_{i-1/2}-u_{i-1/2}\Delta t))}{(x_{i+1/2}-u_{i+1/2}\Delta t)-(x_{i-1/2}-u_{i-1/2}\Delta t)} + x_{i-1/2} \tag{67}$$

At time step t^n, the material m in cell $i-1$ and i are represented by $\Omega^n_{m,i-1}$ and $\Omega^n_{m,i}$, respectively. The notations, $V^n_{-1,i}$ and $V^n_{0,i}$, is the material m in underlying grids with the departure region, as shown in Figure 16. $V^n_{-1,i}$ and $V^n_{0,i}$ satisfy $V^n_{-1,i} = \Omega^n_{m,i-1} \bigcap \Omega^{depart}_i$, and $V^n_{0,i} = \Omega^n_{m,i-1} \bigcap \Omega^{depart}_i$. The regions $V^n_{-1,i}$ and $V^n_{0,i}$ will be advected into the target region and become $V^{n+1}_{-1,i}$ and $V^{n+1}_{0,i}$. Therefore, the volume fraction of material m in the target region Ω_i is

$$F^{n+1}_{m,i} = \frac{\left|V^{n+1}_{-1,i}\right| + \left|V^{n+1}_{0,i}\right|}{\left|\Omega_i\right|} = \frac{\left|T_i(V^n_{-1,i})\right| + \left|T_i(V^n_{0,i})\right|}{\left|\Omega_i\right|} = \frac{\left|T_i(\Omega^n_{m,i-1} \bigcap \Omega^{depart}_i)\right| + \left|T_i(\Omega^n_{m,i} \bigcap \Omega^{depart}_i)\right|}{\left|\Omega_i\right|} \tag{68}$$

The centroid of material m in the target cell Ω_i is

$$\boldsymbol{x}^{n+1}_{m,i} = \frac{\int_{V^{n+1}_{-1,i}} \boldsymbol{x} d\boldsymbol{x} + \int_{V^{n+1}_{-1,i}} \boldsymbol{x} d\boldsymbol{x}}{F^{n+1}_{m,i}\left|\Omega_i\right|} = \frac{\int_{T_i(\Omega^n_{m,i-1} \cap \Omega^{depart}_i)} \boldsymbol{x} d\boldsymbol{x} + \int_{T_i(\Omega^n_{m,i} \cap \Omega^{depart}_i)} \boldsymbol{x} d\boldsymbol{x}}{F^{n+1}_{m,i}\left|\Omega_i\right|} \tag{69}$$

The general volume fraction and centroid of material m at time step t^{n+1} are

$$F^{n+1}_{m,i} = \frac{\sum_{i'=-1}^{1} \left|T_i(\Omega^n_{m,i+i'} \bigcap \Omega^{depart}_i)\right|}{\left|\Omega_i\right|} \tag{70}$$

$$\boldsymbol{x}^{n+1}_{m,i} = \frac{\sum_{i'=-1}^{1} \int_{T_i(\Omega^n_{m,i+i'} \cap \Omega^{depart}_i)} \boldsymbol{x} d\boldsymbol{x}}{F^{n+1}_{m,i}\left|\Omega_i\right|} \tag{71}$$

And the new velocity as a result of advection is

$$\boldsymbol{u}_{m,i}^{advect} = \frac{\sum_{i'=-1}^{1}\int_{\Omega_{m,i+i'}^{n}\cap\Omega_{i}^{depart}} \mathcal{U}_{m,i+i'}^{n}(x)dx}{\sum_{i'=-1}^{+1}\left|\Omega_{m,i+i'}^{n}\cap\Omega_{i}^{depart}\right|\rho_m} \tag{72}$$

here $\mathcal{U}_{m,i+i'}^{n}$ is obtained from MINMOD piecewise linear reconstruction of the momentum (Jemison, 2014).

Since the equations above are only calculated in x direction, the process should be repeated in y and z directions to update the volume fraction, centroid position and advection velocity.

2.5 Approximate Projection Method

The projection method is used as a numerical technique to decouple the computation of velocity $\boldsymbol{u}^{n+1}$ and pressure p^{n+1} at time step t^{n+1}(Chorin, 1968; Temam, 1969). Instead of satisfying the momentum equation and the incompressibility constraint simultaneously, projection method proceeds by first ignoring the incompressibility constraint and computing an intermediate velocity field $\boldsymbol{u}*$ using the momentum equations. Then project $\boldsymbol{u}*$ back to the space of incompressible vector fields to obtain $\boldsymbol{u}^{n+1}$ and p^{n+1}.

The projection method is based on the Ladyzhenskaya theorems (Ladyzhenskaya et al., 1969). Vector $\boldsymbol{u}*$ admits a unique orthogonal decomposition, $\boldsymbol{u}* = \boldsymbol{u}^{n+1} + \nabla\varphi$, where $\boldsymbol{u}^{n+1}$ is solenoidal ($\nabla\cdot\boldsymbol{u}^{n+1} = 0$) and $\nabla\varphi$ is a potential field. According to Temam theorem, any potential vector field $\nabla\varphi$ also has a unique orthogonal decomposition

$\nabla\varphi = \nabla\varphi_0 + \nabla h$ (Chorin, 1969) where $\nabla\varphi_0$ is a potential field and ∇h is solenoidal. Therefore, $\boldsymbol{u}^* = \boldsymbol{u}^{n+1} + \nabla\varphi$ is the unique decomposition where φ is proportional to pressure.

Discretize the momentum equation(41), we obtain

$$\frac{\boldsymbol{u}^{n+1}}{\Delta t} + \frac{\nabla p^{n+1}}{\rho^{n+1}} = \frac{\boldsymbol{u}^n}{\Delta t} - \boldsymbol{u}\cdot\nabla\boldsymbol{u} + \frac{\nabla\cdot(2\mu D)}{\rho} + \boldsymbol{g} - \frac{1}{\rho}\sum_{m=1}^{M}\gamma_m\kappa_m\nabla H(\phi_m) \tag{73}$$

According to the conclusion above, we can obtain

$$\frac{\boldsymbol{u}^*}{\Delta t} = \frac{\boldsymbol{u}^{n+1}}{\Delta t} + \frac{\nabla p^{n+1}}{\rho^{n+1}} \tag{74}$$

$\boldsymbol{u}^*$ could be calculated using equation (73). Take the divergence of equation (74) and since $\nabla\cdot\boldsymbol{u}^{n+1} = 0$ at t^{n+1} we have

$$\nabla\cdot\frac{\nabla p^{n+1}}{\rho^{n+1}} = \frac{\nabla\cdot\boldsymbol{u}^*}{\Delta t} \tag{75}$$

The approximate projection method uses equation (74) and (75) to decouple pressure and velocity. However, the velocity at the cell interface is discretely divergence free and the cell centered velocity is “approximately” divergence free.(Jemison et al., 2013a) The realization of this procedure for the first order scheme can be described in the following steps.

1. The cell center pressure is calculated according to equation (75), where $\boldsymbol{u}^*$ on the cell faces is based on the mass-weighted interpolation to maintain the momentum

conservation (Jemison et al., 2014). Since the cell face value of $\boldsymbol{u}^*$ is used, the cell face value of $\boldsymbol{u}^{n+1}$ is divergence free ($\nabla \cdot \boldsymbol{u}^{n+1} = 0$).

2. The velocity field is then updated with equation (74), $\boldsymbol{u}^{n+1} = \boldsymbol{u}^* - \frac{\nabla p^{n+1}}{\rho^{n+1}}$. The cell face value is also used here for pressure p^{n+1}. The geometric constant contact condition is applied to interpolate p^{n+1} from previous step (Jemison et al., 2014; Kwatra et al., 2009).

2.6 Dynamic Contact Angle Model

In the simulations of droplet impact on the surface, the dynamic contact angle model is applied to model the contact line as a boundary condition. The model of Jiang et al.(Jiang et al., 1979) was used in the study and the value of contact angle depends on the Capillary number. The Jiang's model is derived from experimental measurement by Hoffman(Hoffman, 1975). Since the model of Jiang et al. is valid only for advancing contact angle, Yokoi's model I (Yokoi et al., 2009) is used for receding motion where a constant minimum receding contact angle is obtained from experimental measurement(Zhang et al., 2015).

$$\cos\theta_{\mathrm{m}} = \begin{cases} \cos\theta - (\cos\theta_s + 1)\tanh(4.96 Ca^{0.702}) & Ca \geq 0 \\ \cos\theta_{\mathrm{r}} & Ca < 0 \end{cases} \tag{76}$$

where θ_m is the dynamic contact angle, θ_s is the static contact angle and θ_r is the receding angle. The dynamic contact angle model is also shown in Figure 17.

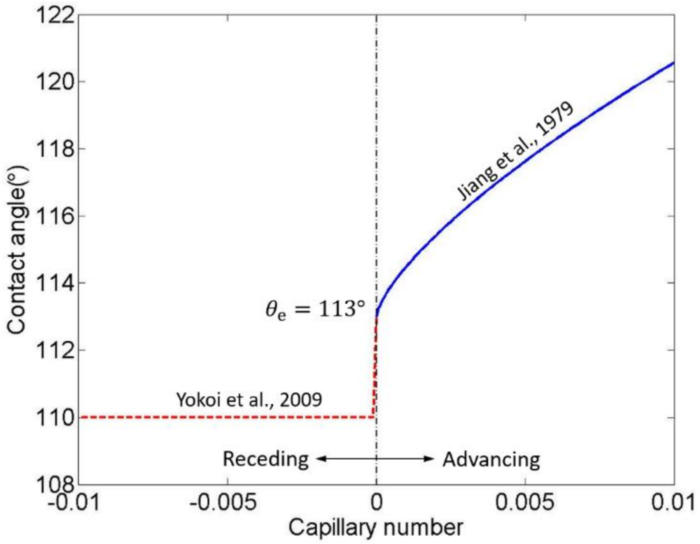

Figure 17 Dynamic contact angle vs. the Capillary number

CHAPTER 3. CODE VALIDATION

A grid sensitivity analysis was conducted before investigating the flow physics. In this analysis, we systematically varied grid densities to study the impact of grid resolution on the droplet coalescence and jumping processes. Computational results, including the coalesced droplet shape and the jumping height of the droplet, were compared with the experimental data(Liu et al., 2014b) to validate the code.

3.1 Computational Setup

The numerical model was validated by comparing with experimental results (Liu et al., 2014b). In the experiment, two initially static water drops with identical radii ($r_0 = 380$ μm) coalesced on a Leidenfrost surface. The Leidenfrost surface was used to approximate the perfectly non-wetting substrate which was believed to be better than textured superhydrophobic surfaces in the experiment (Liu et al., 2014b). When a flat surface was heated to a temperature above the Leidenfrost point (hotter than the liquid's boiling point), an insulating vapor layer with low thermal conductivity was created which kept the liquid drop from boiling and the liquid drop was observed to be floating above the vapor layer (Bernardin et al., 1999; Gottfried et al., 1966; Janssens et al., 2017; Leidenfrost, 1756). In the experiment, the aluminum flat substrate was heated to 250 ± 1℃, significantly higher than the measured Leidenfrost temperature of 195℃ for deionized water drops. The liquid drop floated above the vapor layer with an effective contact angle of 180° (Quéré, 2013). The temperature was measured using thermocouples. The coalescence process was recorded using a high-speed camera with frame rates of up to 6000 f.p.s in order to capture the detailed jumping process. The trajectory of the merged drop was used to extract the jumping velocity using the 'center of mass' based on video images. The axial height (h_z), defined in the inset of Figure 19, was also measured. In our simulation model, the surface was assumed as a perfectly flat substrate with a contact angle of 180˚. The active vaporization from the drops was neglected because the phase-change process is much slower than the jumping process (Liu et al., 2014b). The properties of liquid and air at 100˚C in Table 1 were used during the simulation.

Table 1 The fluid properties assume literature values at 100 ˚C

Contact angle	σ (mN m^{-1})	μ_l (mPa s)	μ_g (mPa s)	ρ_l (kg m^{-3})	ρ_g (kg m^{-3})
180°	58.9	0.282	0.0219	958	0.934

.

Considering the problem being symmetric, we simulated two half-droplets as shown in Figure 18. The computational domain was 1.2 mm by 2.4 mm by 1.6 mm in the x, y, and z directions, respectively. The x-direction is normal to the symmetric plane and the z-direction is perpendicular to the flat substrate surface (z = 0). Also, in the simulation, the symmetric boundary condition was applied at x = 0, a solid wall boundary condition was applied to the flat substrate, and the outflow boundary condition was applied to the rest boundaries.

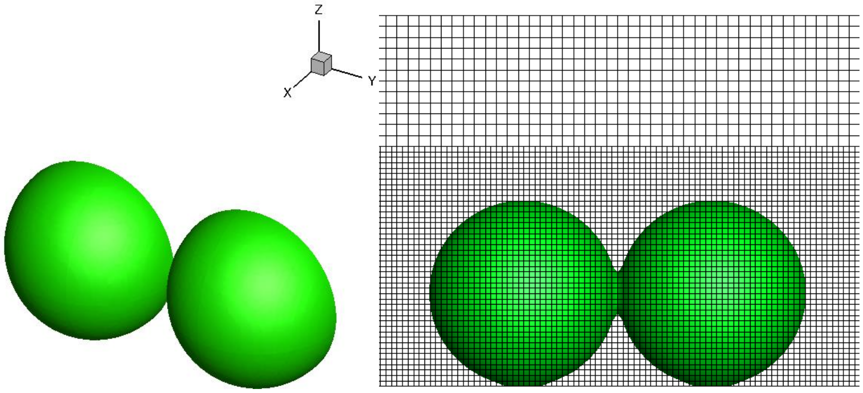

Figure 18 The simulated two drops and the computational grid with one level of refinement. Only half of the domain is simulated because the problem is symmetric with respect to the y-z plane.

3.2 Grid Sensitivity Analysis

Three uniform Cartesian grids were used for the grid sensitivity analysis. The coarse grid had 16, 32 and 24 grid points in the x, y and z directions, respectively. The medium grid had 24, 48, 36 grid points, and the fine grid had 32, 64, and 48 grid points in the x, y and z directions, respectively. In all tests, one level of adaptive mesh refinement was applied (Sussman et al., 1999).

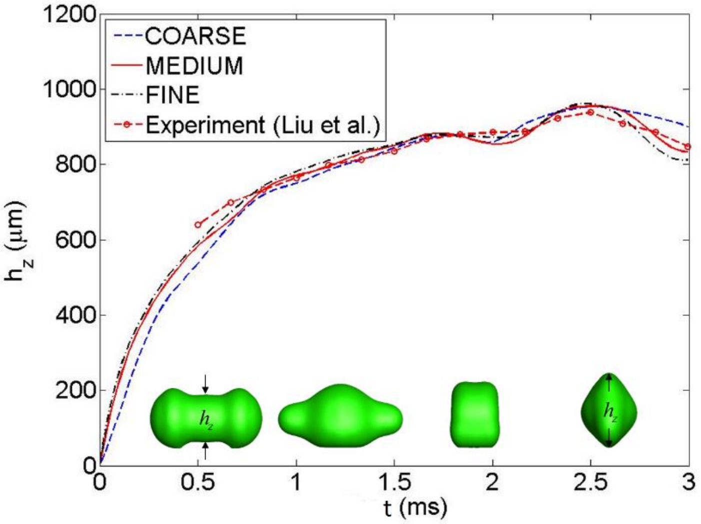

Figure 19 Comparison of vertical axis length (h_z) of the merged drop between simulations and experiment.

The time histories of the vertical axial length change from the three grids are compared in Figure 19. The vertical axial length, h_z , defined in the inset of Figure 19, is the coalesced droplet length with respect to the z-axis. The coarse grid clearly produces a different result than the medium and fine meshes even before t = 0.75 ms. Even though some discrepancies appear after t = 2 ms, results from the medium and fine grids are in overall good agreement. Comparisons were also made with the experimental results (Liu et al., 2014b). The maximum vertical length occurred at t = 2.5 ms in all the simulations, which is consistent with the experiment. Simulation with the coarse mesh diverges from the experiment after t = 2.5 ms but the relative error is still less than 6%. Similarly, the relative error from the medium and fine meshes is less than 4% and 3%, respectively.

All the three grids produced acceptable results in terms of vertical height. However, as shown in Figure 20, at t = 2.7 ms the coarse grid failed to predict the detachment of droplet from the substrate while both the medium and fine grids correctly captured the detachment observed in the experiment. Therefore, the medium grid is used for further study in consideration of both computational accuracy and efficiency.

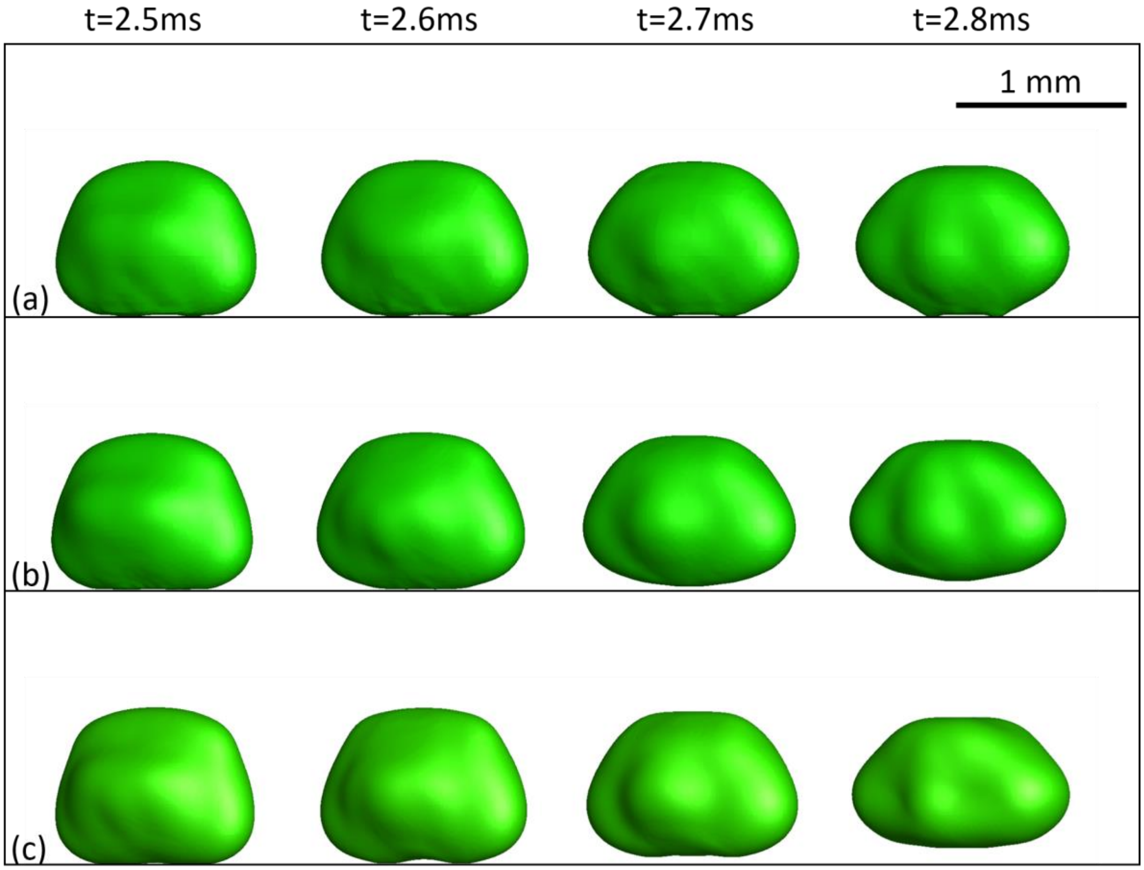

Figure 20 The simulated detachment of droplets from the substrate. The coarse mesh failed to predict the detachment. (a) coarse grid; (b) medium grid; (c) fine grid.

In Figure 21, the coalescence-induced self-propelled jumping process is compared with experimental results. It is clear that our code is capable of accurately capturing the prominent features such as the droplet length in the z-axis direction and the droplet shapes. The slight difference in drop shapes between the simulation and experiment could be due to the simplified contact model, numerical dissipation and other uncertainties.

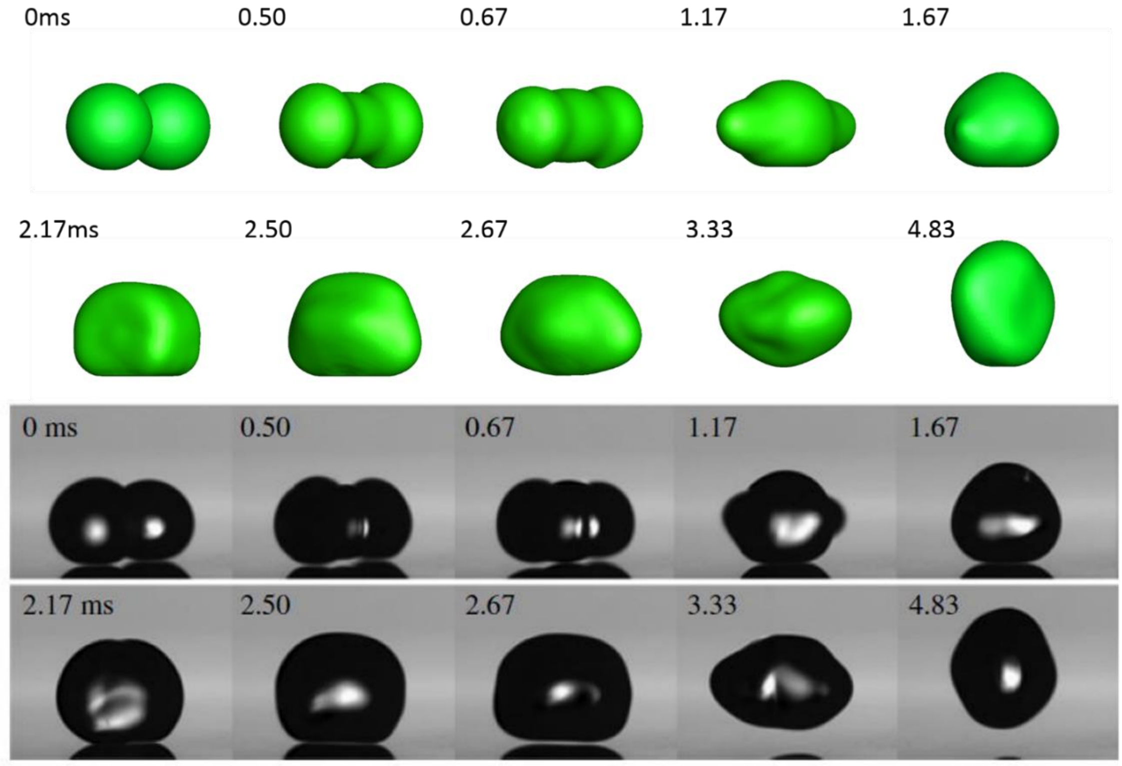

Figure 21 Comparison of simulated jumping motion with the experimental self-propelled jumping process on a Leidenfrost surface

CHAPTER 4. JUMPING MECHANISM ANALYSIS

To illustrate the self-propelled mechanism of the coalesced droplet on the nonwetting substrate, two cases were compared in this chapter. Case 1 has no substrate, i.e., drop coalescence in the air. Case 2 has a flat substrate with contact angle of 180° and droplet coalescence on the substrate. In both cases, the droplets have identical radii of 380 μm. In Case 2 the static contact angle is 180º. The corresponding oscillation period, obtained from Rayleigh frequency(Rayleigh, 1879b), is $T = 2\pi/\sqrt{3}\tau_{ci} \approx 3.4$ ms.

4.1 Five Stages in the Jumping Process

The velocity is represented by $\boldsymbol{u} = (u, v, w)$. u, v and w are velocity components in x, y, and z directions, respectively. We plot the mass-averaged w in Figure 22(a) to investigate the jumping process in Case 2. According to Liu's experiment (Liu et al., 2014a), the jumping process has been divided into four stages. Since the acceleration stage has two distinct accelerations as shown in Figure 22(a), we further divided the acceleration stage into two stages, resulting in a five-stage jumping process. The total five stages are marked in Figure 22(a): stage I (from the beginning to point A) is the expansion of the liquid bridge in the air; stage II (A-B) is the low acceleration stage; stage III (B-C), the high acceleration stage; stage IV (C-D), the departure of the merged drop from the substrate; and stage V (from point D to the end), the deceleration of the departed drop in the air.

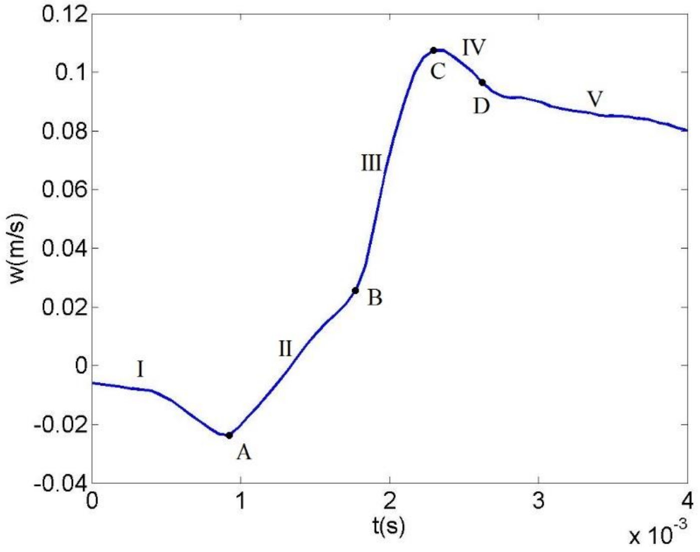

(a) The z-axis velocity vs. time

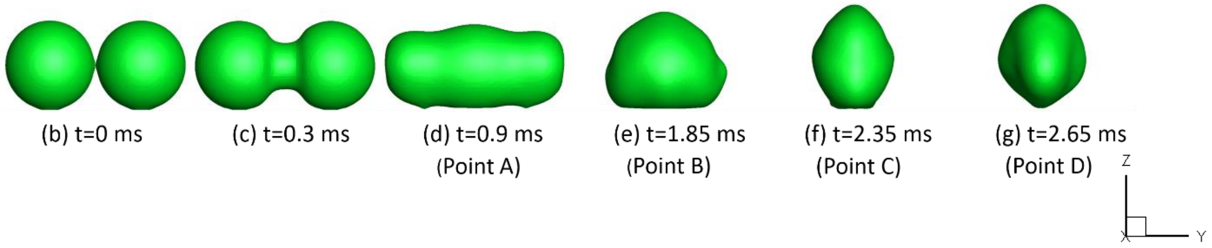

(b) t=0 ms

(c) t=0.3 ms

(d) t=0.9 ms (Point A)

(e) t=1.85 ms (Point B)

(f) t=2.35 ms (Point C)

(g) t=2.65 ms (Point D)

Figure 22 Evolution of the instantaneous droplet during the jumping process: (a) the z-axis velocity; (b)~(g) the droplet shapes during the process

We also marked the end of stage I, II, III and IV as Point A, B, C and D in Figure 22(a). Figure 22(b) ~ (g) depicts droplets' shape evolution during the coalescence-and-jumping process viewed in the x-direction. $Oh = 0.000178$ is obtained from the droplet properties in Table 1, thereby the surface tension and inertia are dominant over the viscosity in the jumping process. At t = 0, the coalescence is triggered by contacting the edges of two adjacent droplets and thereby a liquid bridge is formed between the two drops. At stage I, the capillary pressure, the pressure difference across the interface (Washburn, 1921), drives the flow towards the liquid bridge. The bridge expands axisymmetrically in the x-y plane. At Point A, the liquid bridge contacts the substrate and stage II begins with an acceleration in positive z-direction. An obvious decrease of droplet length in y-direction is observed from Figure 22(d) to Figure 22(e). At Point B, stage III starts with a higher acceleration than stage II. At Point C, the coalesced droplet reaches its maximum speed. During stage IV, the droplet velocity decreases. At Point D (t = 2.65 ms), the droplet detaches from the substrate. After detachment, gravity dominates during stage V and the droplet experiences a lower deceleration than stage IV. The simulated jumping velocity of $w_j = 0.09$ m/s at 2.67 ms agrees with the experimental result of 0.08 m/s at the same time.

4.2 The Velocity Field

To understand how the substrate interrupts the oscillation within the droplet and causes the self-propelled behavior, we compared the velocity vectors of Case 1 and Case 2. According to the characteristics of coalescence, the motion is axisymmetric along y-direction (Sprittles et al., 2012). The velocity vectors on the y-z plane are plotted in Figure 23 and Figure 24 for Case 1 and Case 2, respectively. The droplet shape is shown with solid black lines. During the oscillatory motion in Case 1, both the shape and motion of the droplet can be viewed as symmetric about each middle plane. As shown in Figure 23, the plots are symmetric about x-y plane. However, in Case 2 the symmetry is interrupted beginning at t = 0.9 ms, where the bottom of the droplet begins to contact the surface as shown in Figure 24. The droplet has different accelerations at stage II and III. During the time of stage II and stage III in Case 1, the droplet experiences retraction in y-direction and elongation in z-direction, respectively. At stage II, the top half of the droplet remains the similar shape in Case 2 and the development of vectors is restrained in negative z-direction. At stage III, the whole droplet shape changes. And the vectors gradually change into positive z-direction.

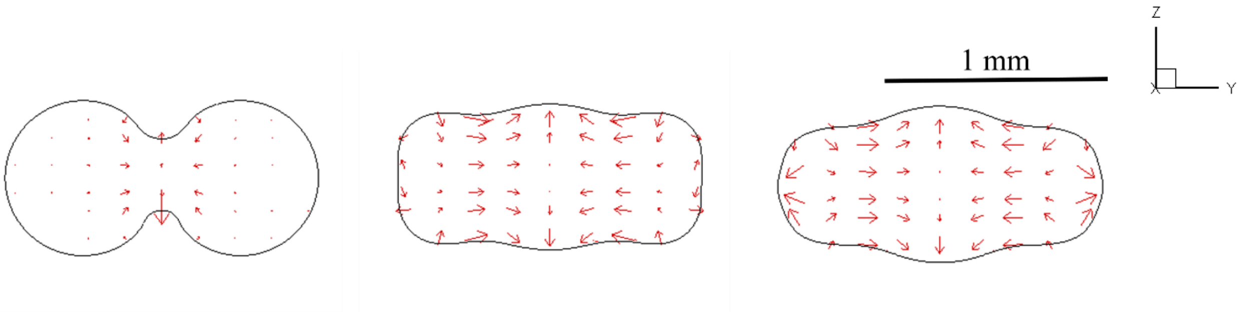

(a) t = 0.3 ms (b) t = 0.9 ms (c) t = 0.95 ms

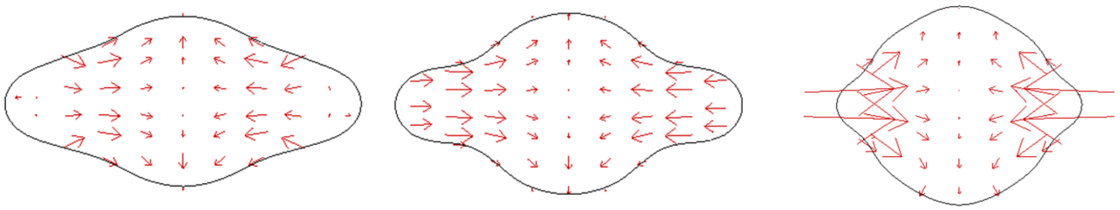

(d) t = 1.25 ms (e) t = 1.45 ms (f) t = 1.85 ms

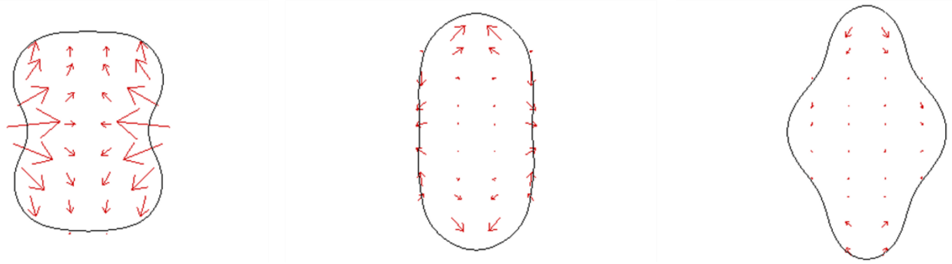

(g) t = 2.10 ms (h) t = 2.35 ms (i) t = 2.65 ms

Figure 23 Velocity vector plots of Case 1 at different time instants (The period of oscillation is approximated to 3.4 ms)

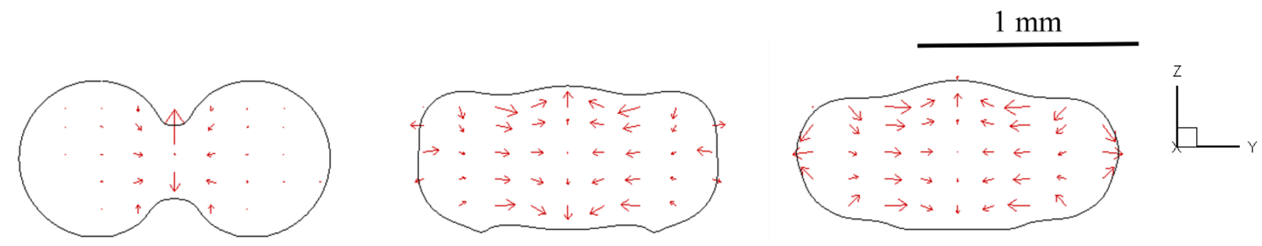

(a) t = 0.30 ms (b) t = 0.90 ms (Point A) (c) t = 0.95 ms

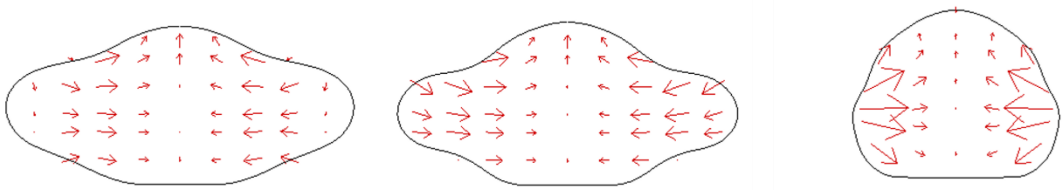

(d) t = 1.25 ms (e) t = 1.45 ms (f) t = 1.85 ms (Point B)

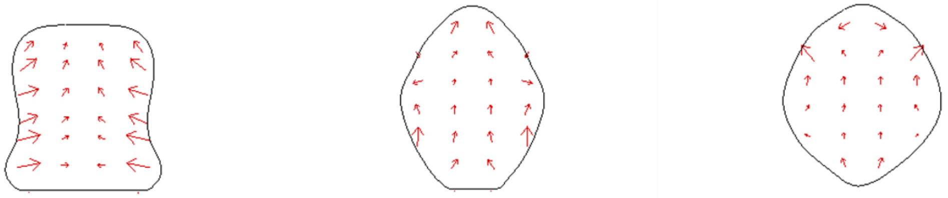

(g) t = 2.10 ms (h) t = 2.35 ms (Point C) (i) t = 2.65 ms (Point D)

Figure 24 Velocity vector plots of Case 2 at different time instants

4.3 The z-axis Momentum

To further investigate how the symmetric motion is interrupted, we compared the time history of momentum in the z-direction between Case 1 and Case 2. The z-axis momentum was integrated based on the direction. The $z+$ momentum is the integration of the momentum only in positive z-direction and $z-$ momentum is the integration only in negative z-direction. The $+$ and $-$ represent the direction of momentum. In Figure 25, the $z+$ and $z-$ momentum of Case 2 are plotted with red solid and dashed lines, respectively; and the $z+$ and $z-$ momentum plots of Case 1 are blue solid and dashed lines marked with circles. Without the presence of a substrate, the $z+$ and $z-$

momentum plots of Case 1 are symmetric about 0-momentum line. In Case 2, the substrate results in an asymmetrical distribution of z-axis momentum.

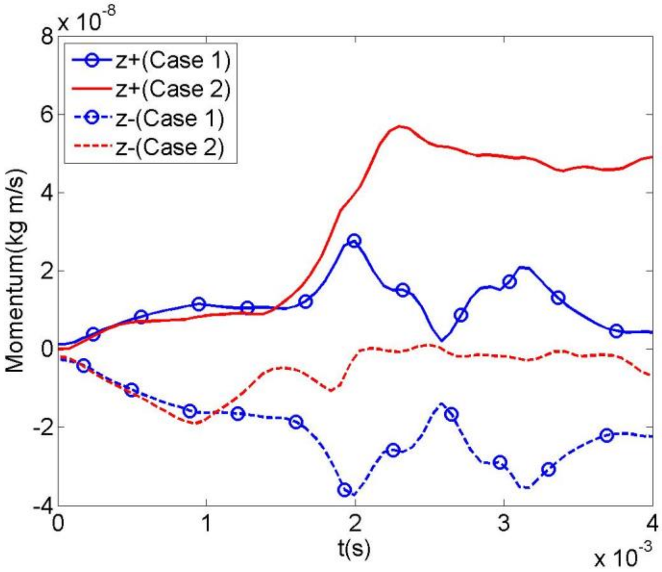

Figure 25 Comparison of positive and negative momentums of Case 1 and Case 2

The momentum plots of Case 1 and Case 2 have similar trends at stage I. At t = 0.9 ms, the liquid bridge in Case 2 contacts the substrate, which suppresses the further development of the $z-$ momentum. The $z+$ momentum of the two cases has similar development at stage II. From t = 1.45 ms to t =1.85 ms, the magnitude of both $z+$ and $z-$ momentum has a rapid increase in Case 2 due to the surface energy released from the strong retraction in y-direction. At beginning of stage III, the $z-$ momentum is suppressed by the substrate again. The sum of $z-$ momentum suppression and $z+$ momentum acceleration gave a higher acceleration at stage III than at stage II. From then on, the negative z momentum is close to 0 until the drop detaches from the substrate.

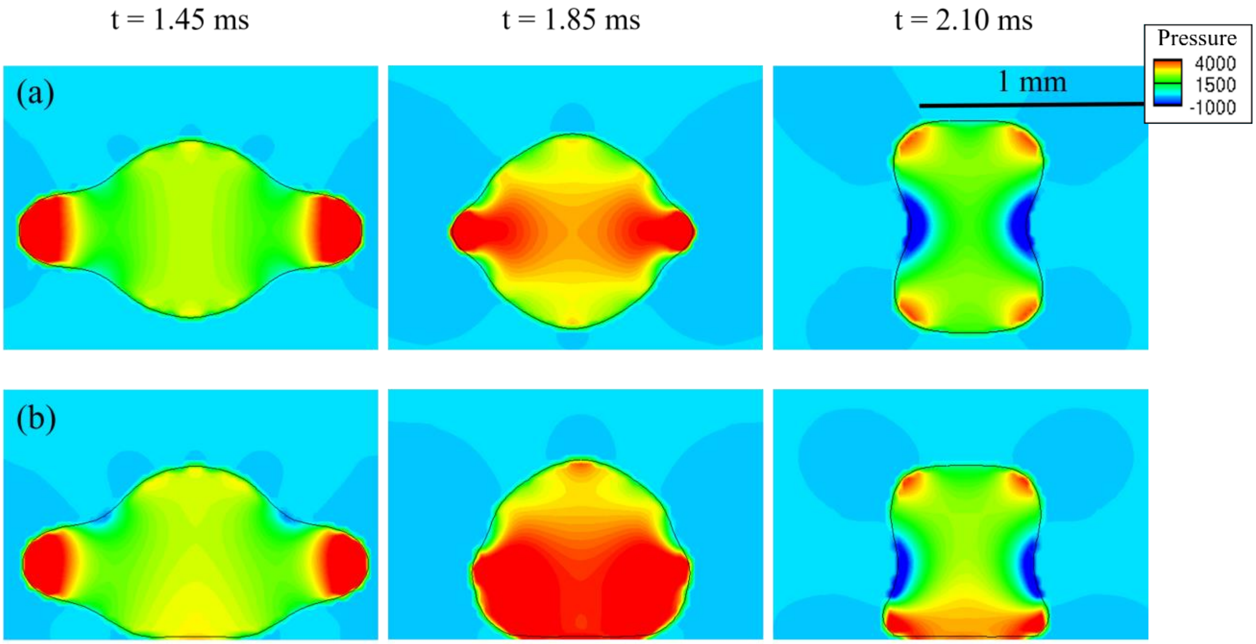

Figure 26 Pressure gradient in the droplet during jumping speed acceleration: (a) Case 1; (b) Case 2.

At around t = 2 ms, the positive z-axis momentum plot of Case 2 continues to increase after the magnitude of z+/- momentum in Case 1 reaches the maximum value. This is due to the high-pressure area at the bottom of the droplet, as shown in Figure 26(b). The high-pressure area in Case 1 is in the middle of the droplet at t = 1.85 ms and evenly affect both top and bottom of the droplet. The high-pressure area vanishes at t = 2.1 ms. In Case 2, the substrate prevents the droplet development in negative z-direction resulting in the high-pressure area at the bottom of the droplet. And the high pressure in the bottom still exists at t = 2.1 ms and the droplet continnues moving upward.

4.4 Energy Conversion Analysis

In Figure 28 we plot the time histories of the changes in the surface energy (ΔE_s) and kinetic energy (ΔE_k) of both Case 1 and Case 2. The beginning of the surface energy and kinetic energy are set as 0. The black dash inset marks the time when the droplet is detaching from the substrate in Case 2. The maximum decrease of surface energy happens at around t = 1.85 ms (Point B) when the surface area of droplets is minimum, and the decrease of surface energy in Case 2 is less than Case 1. At the same time, the maximum increase in kinetic energy occurs, and the increment in Case 2 is less than Case 1.

During droplet detachment (from t = 2.35 ms to 2.65 ms), ΔE_s in Case 2 is lower than in Case 1 which means the droplets in Case 2 has a smaller surface area. Comparing the droplet shapes in Figure 23 and Figure 24, the droplet is more elongated in Case 1. As a result, more energy exists as kinetic energy in Case 2. Beginning at t = 2.10 ms, more energy is dissipated in Case 2 than in Case 1 as shown in Figure 28. The high-pressure zone in the droplet pushes the bottom half droplet upward which is opposite from the original oscillation and creates more chaos in the droplet.

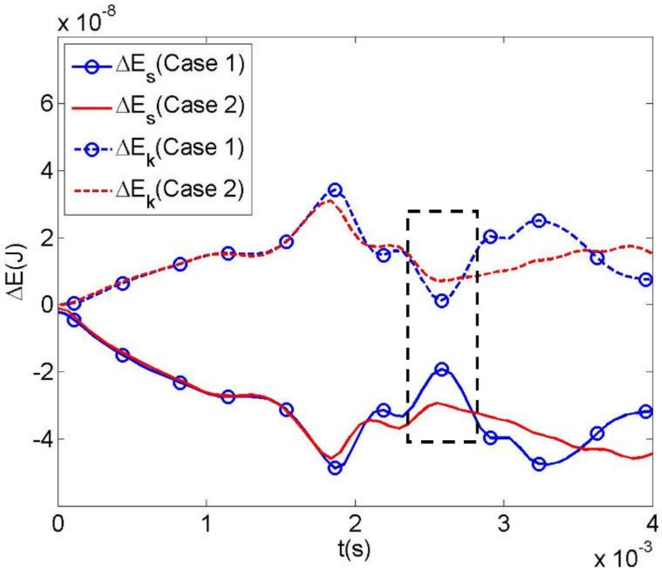

Figure 27 Time histories of changes in total kinetic energy and surface energy of Case 1 and Case 2, ΔE_s and ΔE_k represent surface energy and total kinetic energy, respectively

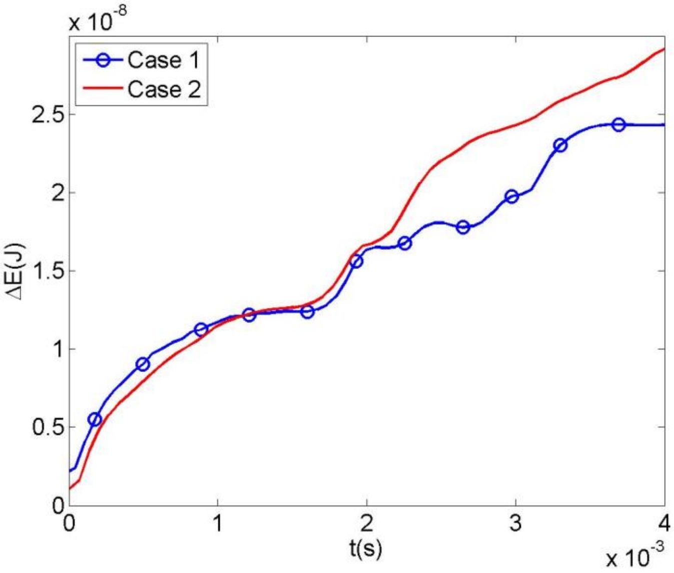

Figure 28 Comparison of dissipation energy changes of Case 1 and Case 2

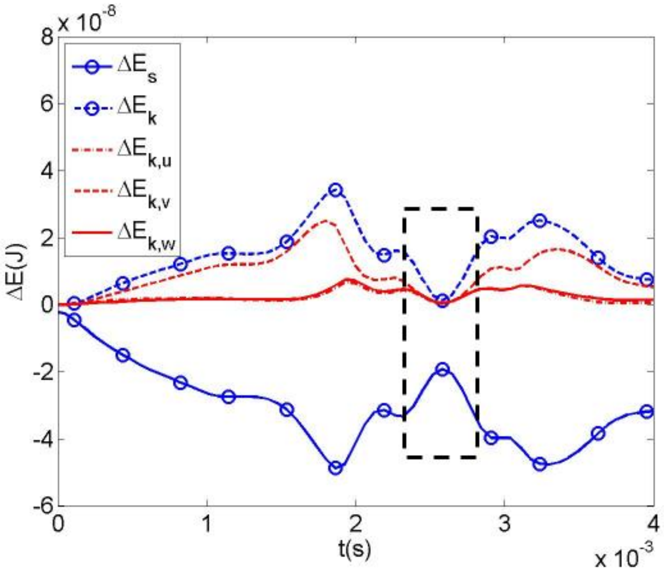

(a) Case 1

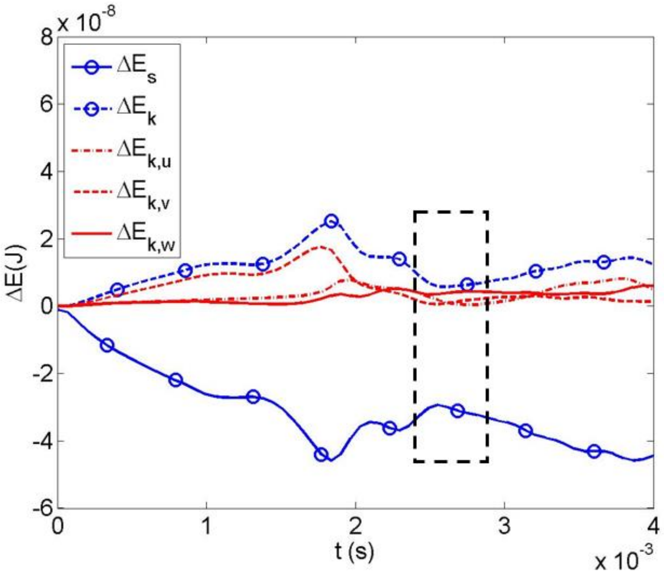

(b) Case 2

Figure 29 The distribution of energy changes during droplets coalescence: (a) Case 1; (b) Case 2. ΔE_s and ΔE_k, represent surface energy, total kinetic energy, respectively. $\Delta E_{k,u}$, $\Delta E_{k,v}$ and $\Delta E_{k,w}$ further represent the kinetic energy due to u, v and w.

In Figure 29 we plot the changes in the surface energy and kinetic energy due to the velocity in each direction of both Case 1 and Case 2. In Case 1, $\Delta E_{k,v}$ accounts for the majority of the kinetic energy change. $\Delta E_{k,w}$ is almost coincided with $\Delta E_{k,u}$ in Figure 29 (a). At t = 2.65 ms, $\Delta E_{k,u}$, $\Delta E_{k,v}$ and $\Delta E_{k,w}$ reach their minimum values simultaneously when ΔE_s reaches its maximum value during the expansion.

In Figure 29 (b), $\Delta E_{k,v}$ of Case 2 also accounts for the majority of the kinetic energy change in the beginning. However, the energy conversion between surface and kinetic energy of Case 2 later shows differences from Case 1 due to the substrate effect. The change in kinetic energy of Case 2 shows a similar trend at t = 2.65 ms. But ΔE_k in Case 2 is higher than in Case 1 (Figure 27). $\Delta E_{k,w}$ occupies the majority of the kinetic energy in Case 2, as shown in Figure 29(b). And only $z+$ momentum exists during the detachment (Figure 25).

CHAPTER 5. EFFECTS OF DROPLET PROPERTIES

The effects of droplet size, surface tension and droplet density on the jumping process are investigated in this chapter. In the plots time is nondimensionalized by the characteristic time $\tau_j = \sqrt{\rho_l r_0^3 / \sigma}$, velocity by capillary-inertia velocity, u_{ci} , and energy by $\rho_l (\frac{8}{3}\pi r_0^3) u_{ci}^2$. The approaching speed on the jumping process is investigated and the dimensionless constants is introduced in the analysis.

5.1 Droplet Size

Droplets with radii of 10μm, 100μm, 380μm were studied and compared. Figure 30 Droplets with radii of 10μm, 100μm, 380μm were studied and compared. compares the dimensionless jumping speed over dimensionless time. Even though a smaller radius leads to higher jumping velocity. as indicated capillary-inertial scaling law, in the dimensionless plots, the three cases are very similar to each other and they all obey the capillary inertial scaling $w_j \sim r_0^{-1/2}$. The dimensionless velocity contours in the z-direction are also plotted in Figure 31. The droplet shapes and the velocity distributions are nearly identical for the three cases. It should be noted that, since the larger droplet has a larger characteristic time, for the same dimensionless scale, the dimensional time of the larger droplet will be larger.

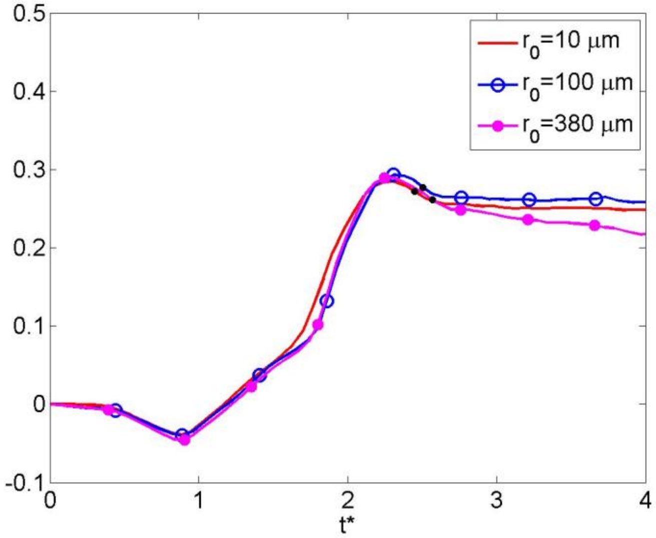

Figure 30 Comparison of dimensionless jumping velocity at different initial radii.

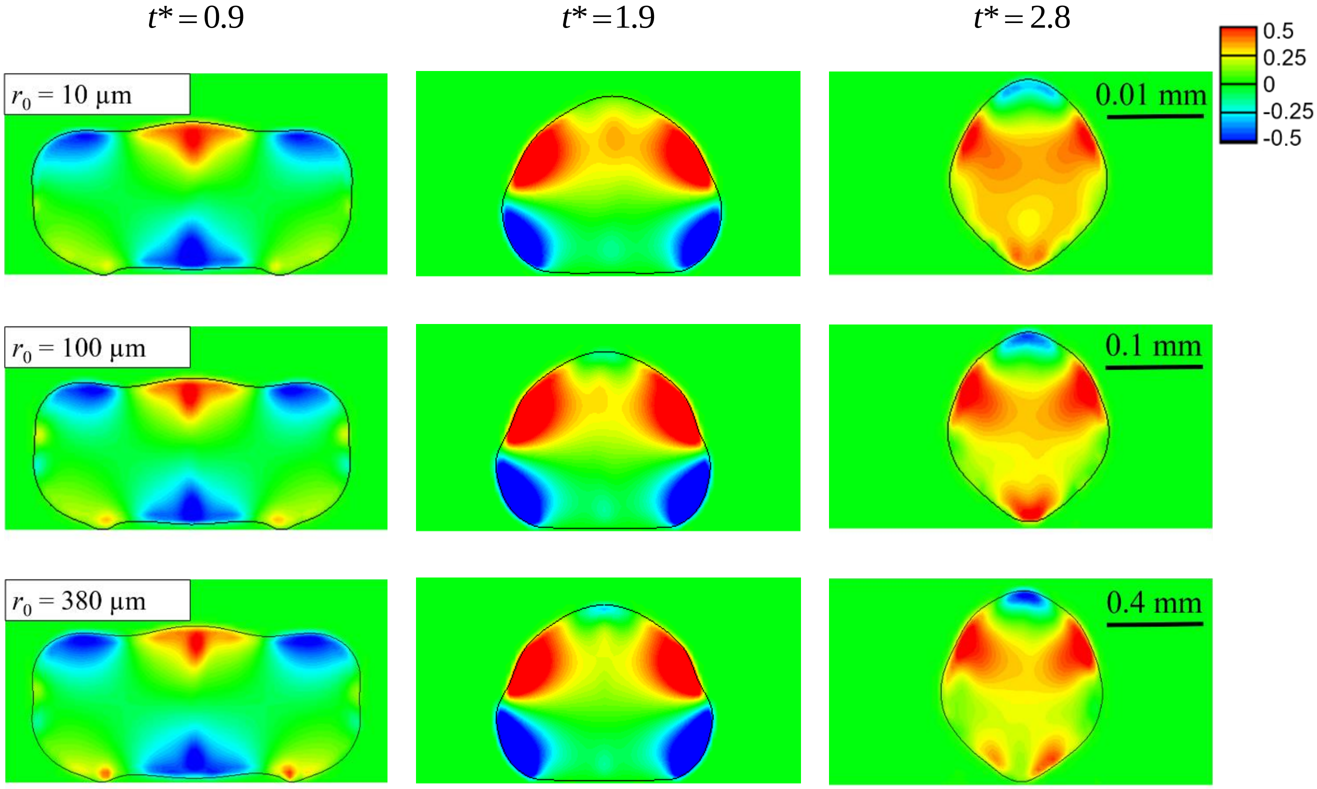

Figure 31 Comparison of the droplet deformation and dimensionless z-axis velocity contours with the initial radii of 10μm, 100μm and 380μm

The dimensionless kinetic energy (E_k^*) and surface energy (E_s^*) are plotted and compared for in Figure 32. The three cases show very similar patterns.

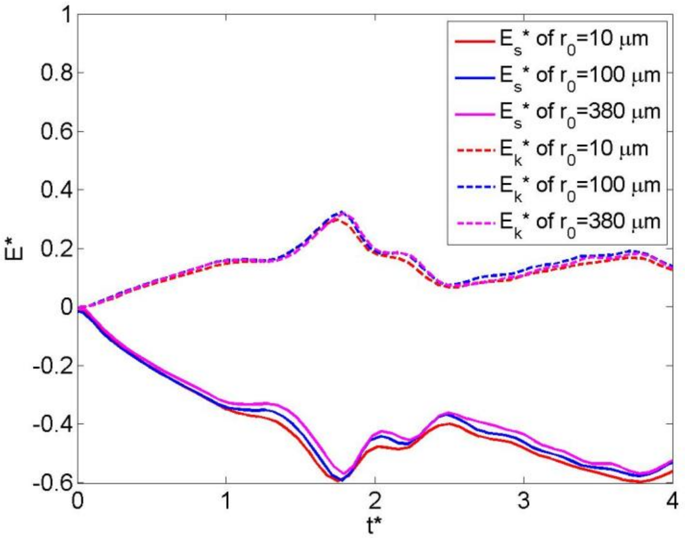

Figure 32 Surface and kinetic energy plot of droplets with radii of 10 μm, 100 μm and 380 μm

In Figure 33 the jumping speed is compared with the empirical models from experiments(Enright et al., 2013; Liu et al., 2014b). It is clear the jump speed increases with the decrease of initial drop radius. Our simulation results are close to the empirical models. Based on our simulation, the 3% ~ 6% of the released surface energy is converted to kinetic energy in the vertical direction.

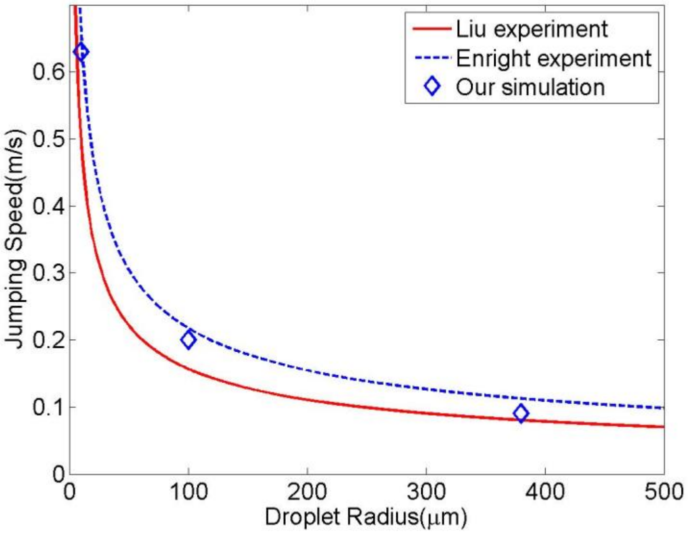

Figure 33 Jumping speed vs. the droplet size compared with empirical models (Boreyko et al., 2009; Liu et al., 2014b)

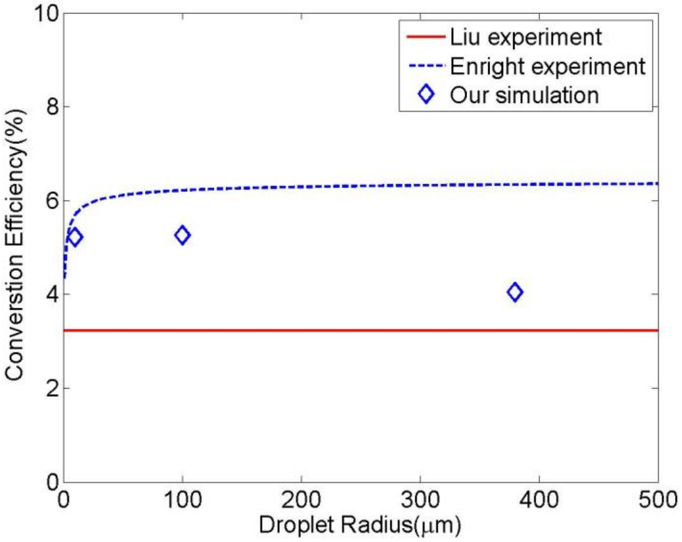

Figure 34 Energy conversion speed plot vs. the droplet size and comparison with results based on empirical models (Boreyko et al., 2009; Liu et al., 2014b)

5.2 Droplet Density

Density effect was investigated by varying the droplet density. Three densities, $479\ \mathrm{kg\ m^{-3}}$, $958\ \mathrm{kg\ m^{-3}}$, and $1916\ \mathrm{kg\ m^{-3}}$ were tested. The jumping speed obeys the capillary-inertial scaling law $w_j \sim \rho_l^{-1/2}$. The three cases show nearly identical results in terms of dimensionless surface and kinetic energy. There is no significant difference in terms of the droplet deformation and dimensionless jump speed among the three cases as shown Figure 35.

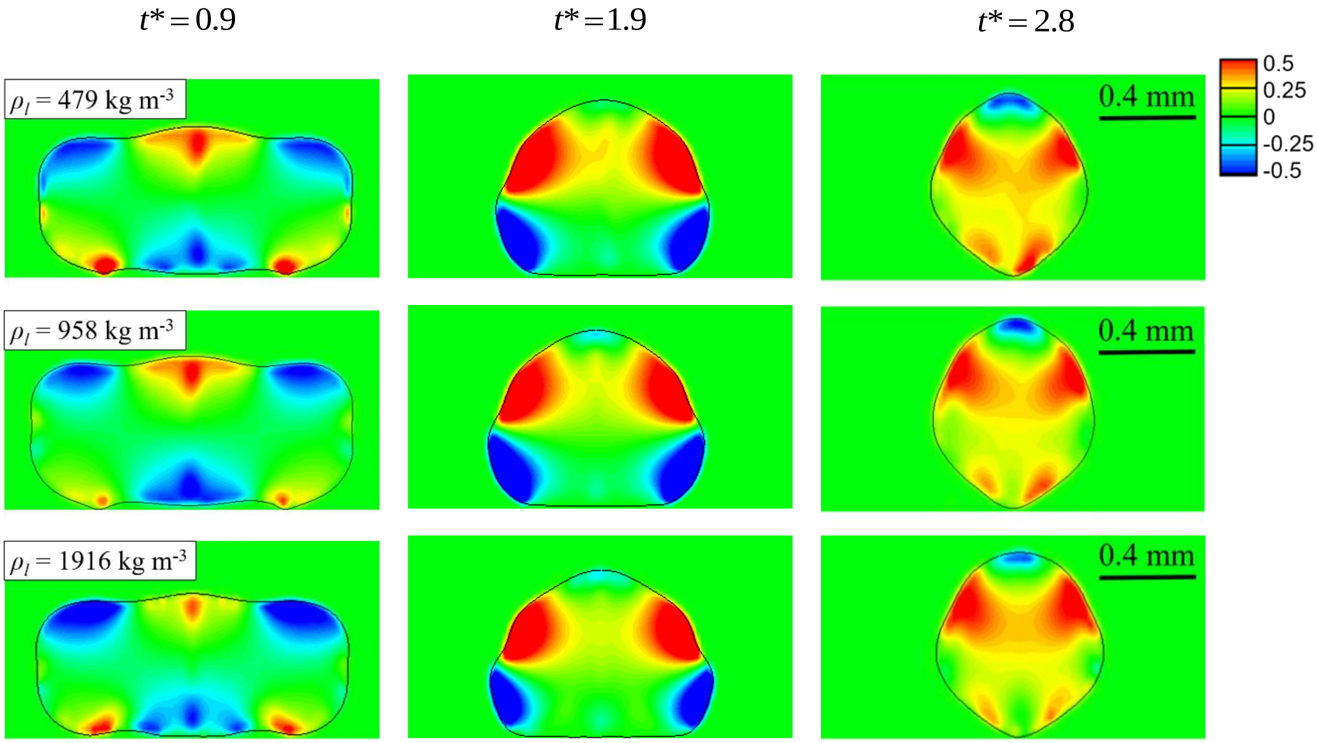

Figure 35 Comparison of the droplet deformation and dimensionless z-axis velocity contours with the density of $0.5\rho_0$, ρ_0 and $2\rho_0$

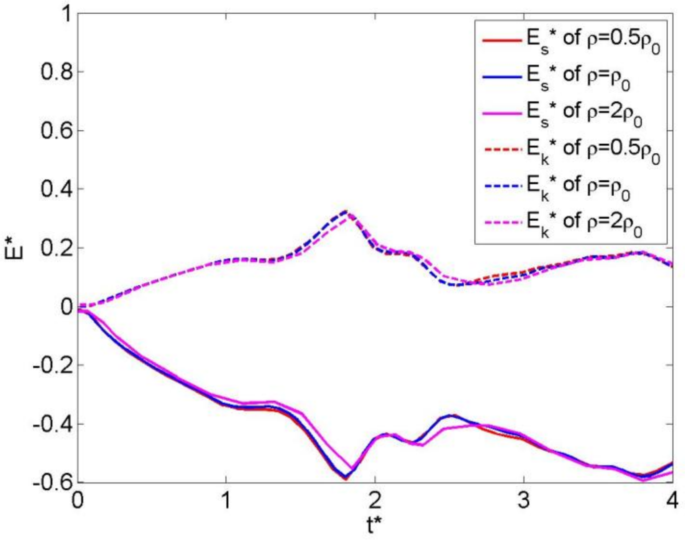

Figure 36 Surface and kinetic energy plot of droplets with the density of $0.5\rho_0$, ρ_0 and $2\rho_0$

5.3 Surface Tension

Comparisons were also made to understand the surface tension effect. We tested three surface tensions: 29.5 mN m^{-1}, 58.9 mN m^{-1} and 117.8 mN m^{-1}. As shown in Figure 37 the three cases show nearly identical results in terms of the dimensionless jumping speed. Since the droplet with lower surface tension has a larger characteristic time, for the same dimensionless scale, the dimensional time of the droplet with lower surface tension will be larger.

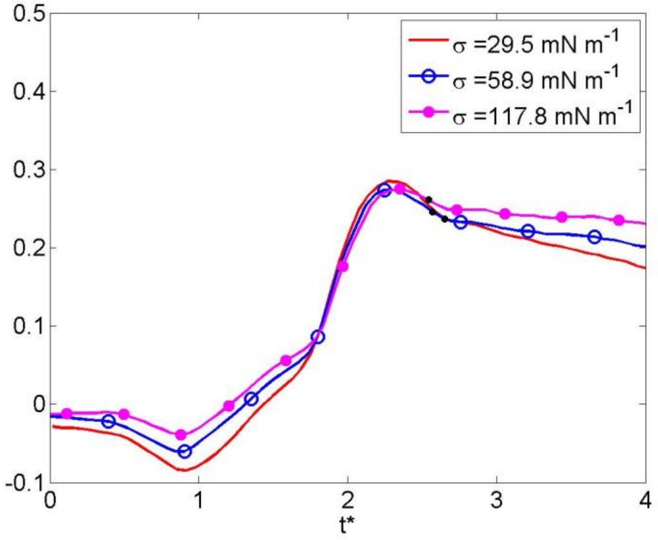

Figure 37 The instantaneous vertical speed (z axis) plot during the jumping process for droplets with the surface tension of $0.5\sigma_0$, σ_0 and $2\sigma_0$

5.4 Approaching Speed

Liu et al.(Liu et al., 2014b) claimed that the jumping velocity is independent of the relative approaching velocity orthogonal to the jumping direction. However, the approaching speed was defined as relative speed between the two droplets. As depicted in Figure 38, only the speed in y-direction is taken into consideration ($v_{rel} = \left|v_{y,r} - v_{y,l}\right|$).

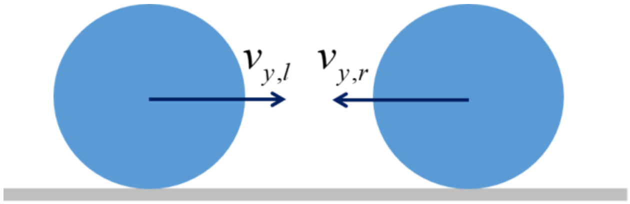

Figure 38 Illustration of the approaching speed between two droplets

In this study, two relatively high approaching speeds (1 m/s, and 2 m/s) were used leading to the Weber number of 6.5 and 26. The nondimensionalized jumping velocities are compared in Figure 39. Time is nondimensionalized by the jumping period (from the beginning of coalescence to the drop detaching from the substrate). The jumping periods are 2.6 ms, 1.6 ms and 1.3 ms for the approaching speed of 0, 1 and 2 m/s, respectively. Higher jumping velocity is observed for the droplet with $v_{rel} = 2$ m/s. However, the droplet with $v_{rel} = 1$ m/s shows lower jumping velocity than the case of $v_{rel} = 0$.

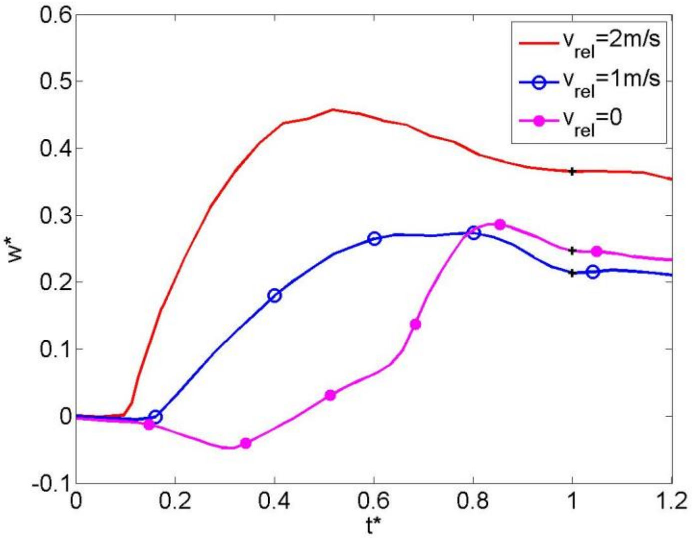

Figure 39 Comparison of jumping velocity at different approaching velocities

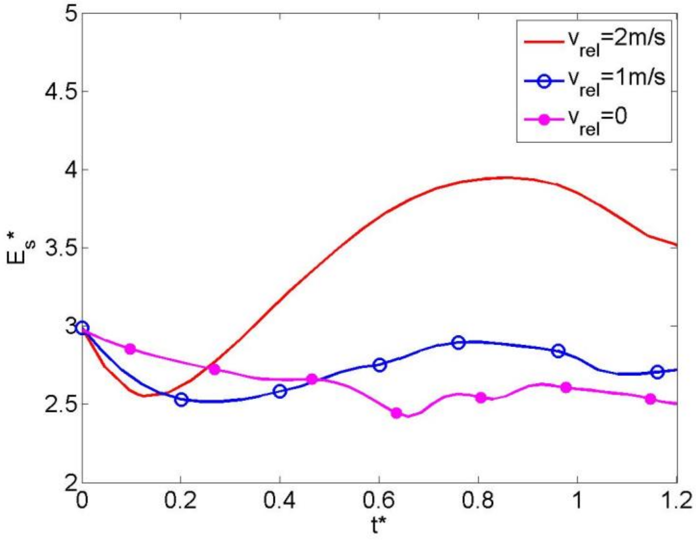

(a) Surface energy

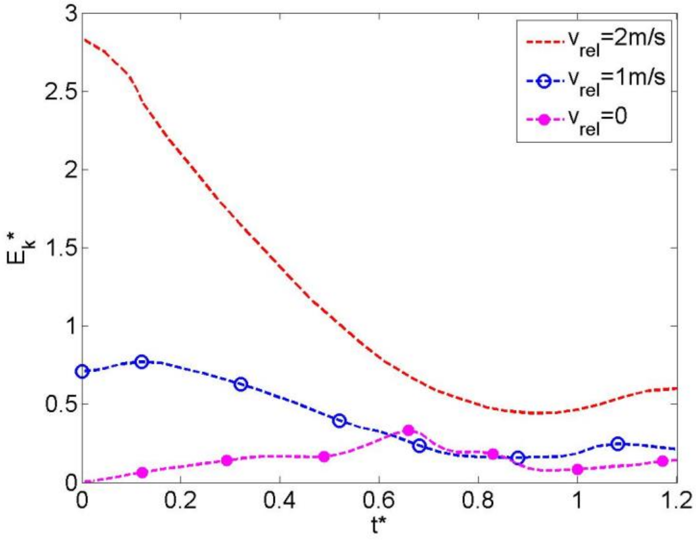

(b) Kinetic energy

Figure 40 Comparison of energy change of the cases at different approaching speeds

We compare the dimensionless surface energy, kinetic energy and dissipation energy during the process in Figure 40 and Figure 41. All the cases experience decreases in surface energy at the beginning of the coalescence as shown in Figure 40(a). The two cases with approaching speeds of 1 m/s and 2 m/s have a short time of decrease in surface energy and the decrease ends earlier for $v_{rel} = 2$ m/s. After that, the surface energy keeps increasing until droplet detaching from the substrate. The surface energy increase with the approaching velocity. The surface energy of $v_{rel} = 2$ m/s is even higher than at t* = 0. In Figure 40 (b), the kinetic energy at t* = 0 is different due to the existence of approaching speed. Both cases for $v_{rel} = 0$ and $v_{rel} = 1$ m/s experience increase in the kinetic energy at the beginning. The kinetic energy for $v_{rel} = 2$ m/s keeps decreasing from t* = 0 to the moment droplet detaching from the substrate. The energy dissipation of each case increases with respect to the approaching speed as shown in Figure 41.

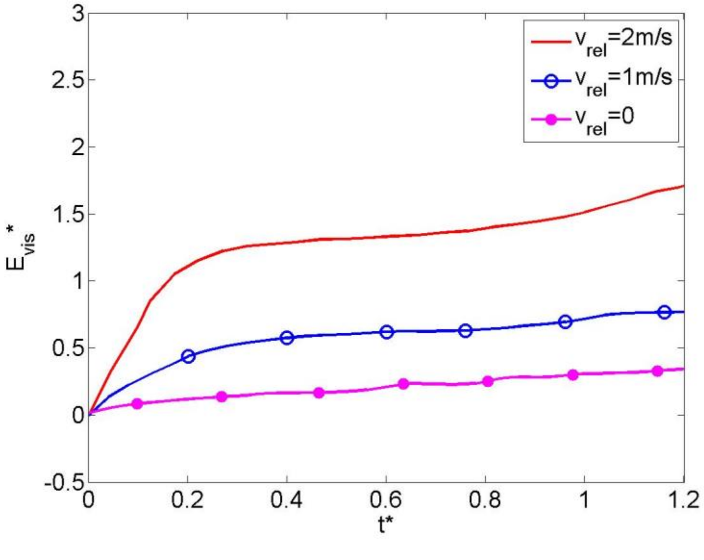

Figure 41 Comparison of energy dissipation energy of the cases at different approaching speeds

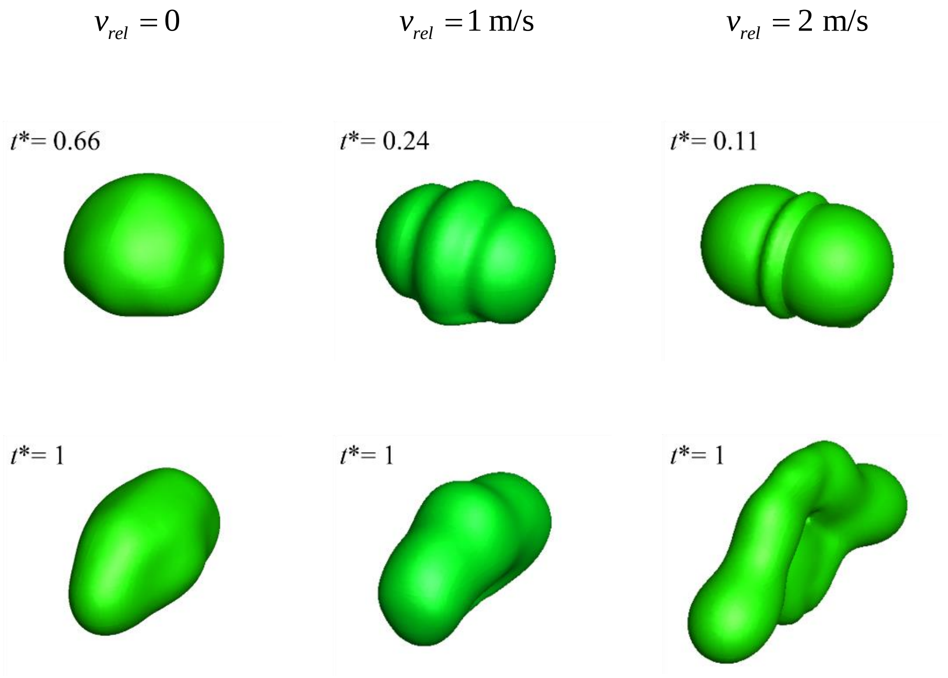

Figure 42 Droplet shapes at different approaching speed

We also plot the droplet shapes at the moment of lowest surface energy and at the moment of the detachment. At the moment of lowest surface energy, the cases with approaching speed have relatively more deformed shape. The larger curvature appears on the surface of $v_{rel} = 2$ m/s. At the detaching moment, the droplet shape is also more deformed in the case with larger approaching speed. The velocity z-direction velocity contours on the y-z plane of the three cases are plotted at the two moments in Figure 43.

The cases of $v_{rel} = 2$ m/s and $v_{rel} = 1$ m/s have relatively similar deformed shapes and velocity distribution.

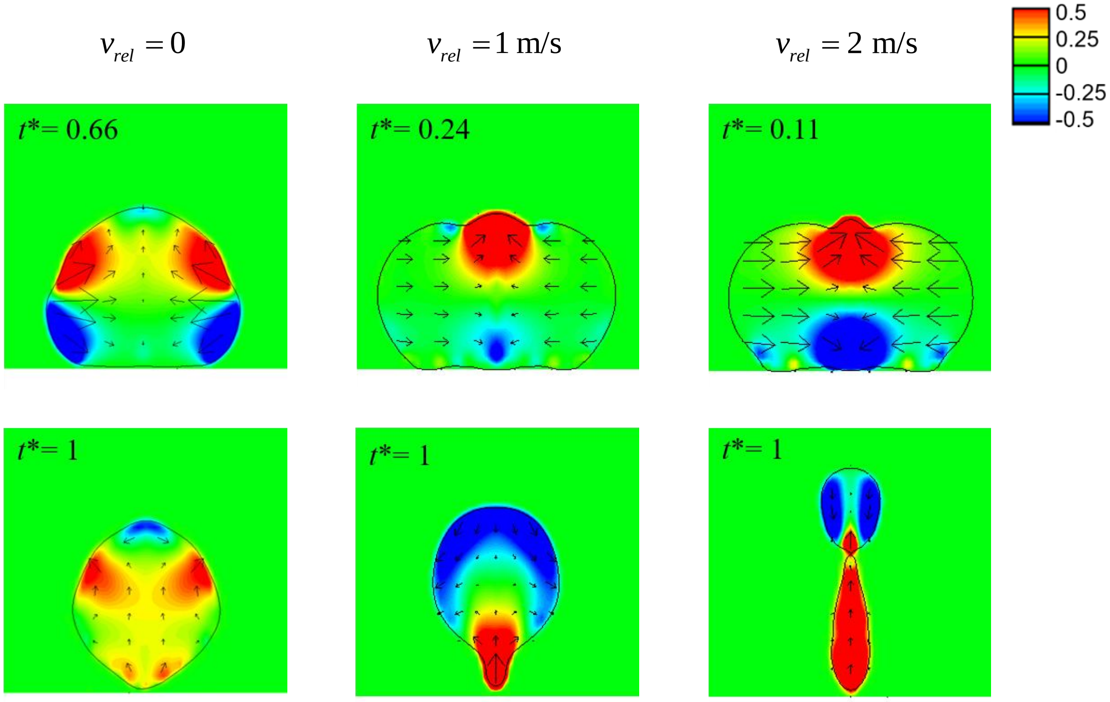

Figure 43 Droplet deformation during the process at different approaching speeds

CHAPTER 6. SUBSTRATE SURFACE EFFECT

The coalescence induced jumping behavior is numerically investigated on the wedged surface. The code is validated by comparing with experimental results from two different cases. Then we investigate the effects of curvature by simulating the droplet coalescence on wedged surfaces. The curvature of wedge on the surfaces is $\kappa = 1/(0.2r_0)$, $\kappa = 1/(0.4r_0)$, $\kappa = 1/r_0$ and $\kappa = 0$ (flat surface) with the contact angle of 180°. The surface adhesion is investigated by varying the contact angles at 90°, 110° and 180°. The contact angle is modeled with dynamic contact angle in the study.

6.1 Code Validation

The droplet coalescence on a flat substrate was already validated in Chapter III. Two more validation cases, related with the wedged surfaces, are presented in this section. The first case is a single droplet bouncing-off on a curved surface. The second case is two droplets coalescence on a fiber.

6.1.1 Drop Bouncing on Convex Surface

In the first case, we validate the code with the experiment of drop bouncing on a convex surface. The experiment was conducted by Liu et al.(Liu et al., 2015) with a drop impinging on the convex surface of Echeveria leaf. The same drop bouncing was conducted on a flat surface for the purpose of comparison. The water properties at 20°C in Table 2 is used in the validation case. The droplet diameter is 2.9 mm and the diameter of the convex surface is 8.2 mm. The impact velocity of the droplet is 0.63 m/s corresponding to We = 7.9 (Weber number), and Oh = 0.0028 (Ohnesorge number). The contact angle of the surface is 160˚.

Table 2 The fluid properties assume literature values at either 20 ˚C or 100 ˚C

	σ (mN m^{-1})	μ_l (mPa s)	μ_g (mPa s)	ρ_l (kg m^{-3})	ρ_g (kg m^{-3})
20˚C	72.7	1.071	0.0182	998	1.190
100˚C	58.9	0.282	0.0219	958	0.934

The experimental and numerical results of the droplet bouncing process on the convex surface are compared in Figure 44. And the comparison on the flat surface is shown in Figure 45. The simulation shows good agreement with the experimental result. The simulation can predict the droplet deformation and can also capture the moment that the droplet bounces off the curved surface. An anisotropic bouncing is captured on a convex surface and the contact time is 40% less than on a flat surface. The contact time increases with the diameter of curvature (Liu et al., 2015). The anisotropic bouncing was believed to be the reason that the droplet had less contact time on the convex surface than on the flat surface (Liu et al., 2015).

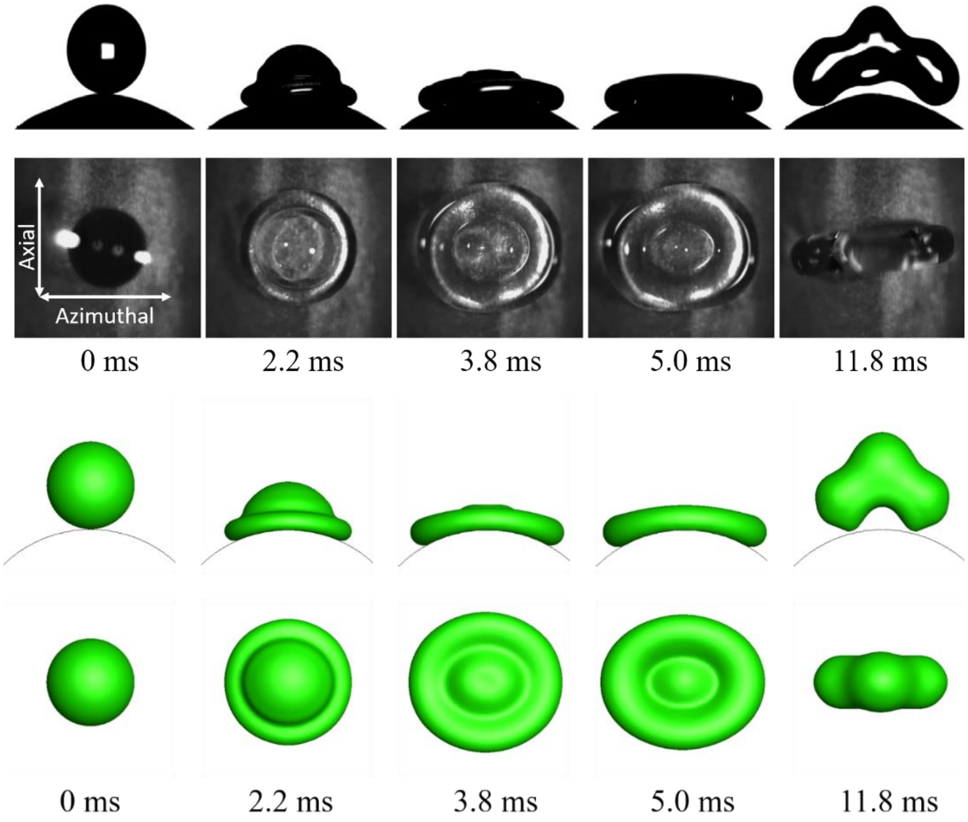

Figure 44 Comparison of experimental results(Liu et al., 2015) and simulation results of single droplet bouncing off on the curved surface

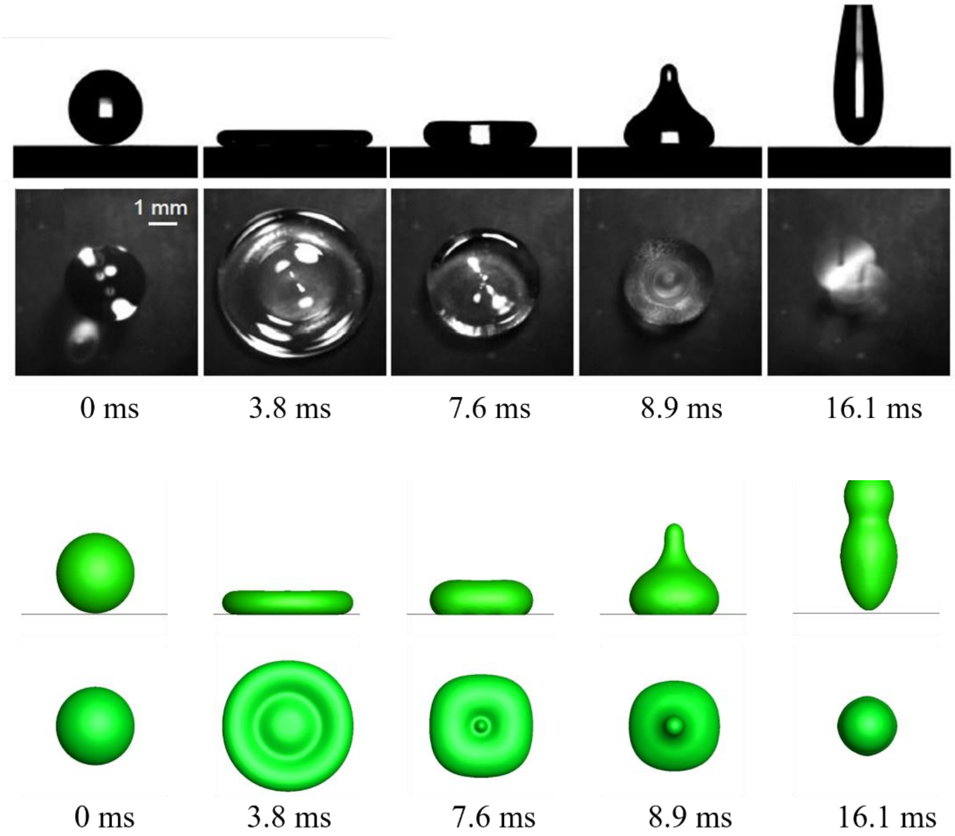

Figure 45 Comparison of experimental results(Liu et al., 2015) and simulation results of single droplet bouncing off on the flat surface

For a conventional bouncing, as shown in Figure 45, the drop spreads, forms some kind of a pancake and finally retracts to bounce-off. Both the spread and retraction are isotropic. In Figure 44, the drop on the convex surface experiences an anisotropic spread and the impact area is approximately elliptical which leads less momentum transferred in the azimuthal direction than in the axial direction. The drop undergoes faster retraction in axial direction resulting an uneven distribution of momentum and mass distribution between axial direction and azimuthal direction. At t = 11.8 ms, the drop retracts to the minimum in axial direction which leads to the droplet bounce-off.

6.1.2 Coalescence-induced Self-bouncing on a Fiber

In the second case, we validate the code for coalescence induced droplet self-bouncing phenomenon on a fiber with contact angles of $\theta_A / \theta_R = 120° / 110°$. The radius of the droplet is 249 μm and the radius of the fiber is 46 μm. The water properties at 20 ˚C in Table 2 is adopted for the purpose of this code validation. Figure 46 compares the experimental and numerical results during the self-bouncing process on the fiber. The two droplets coalesce, deforms around the fiber and detaches from the fiber. The simulation can capture droplet shapes during coalescence and bouncing behavior on the fiber.

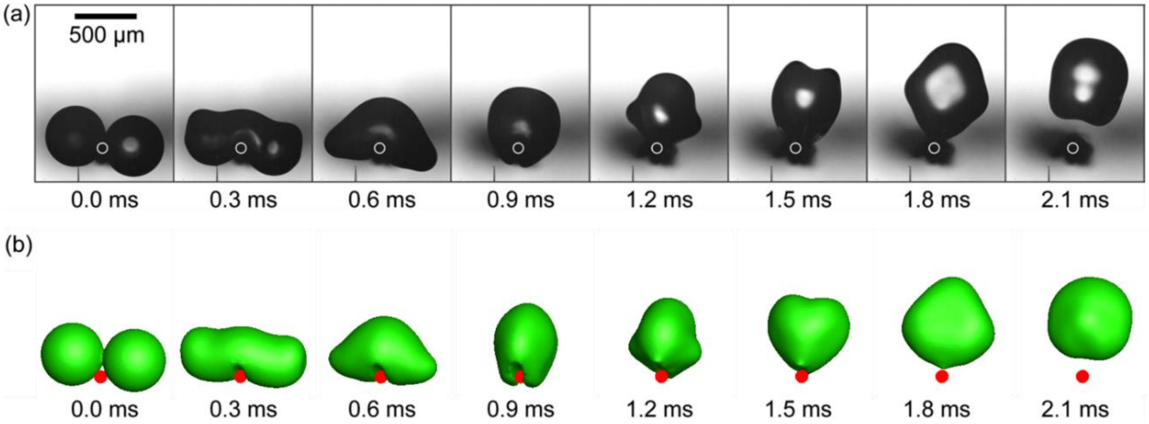

Figure 46 Comparison of experimental results(Liu et al., 2015) and simulation results of coalescence induced droplet self-bouncing behavior on the fiber

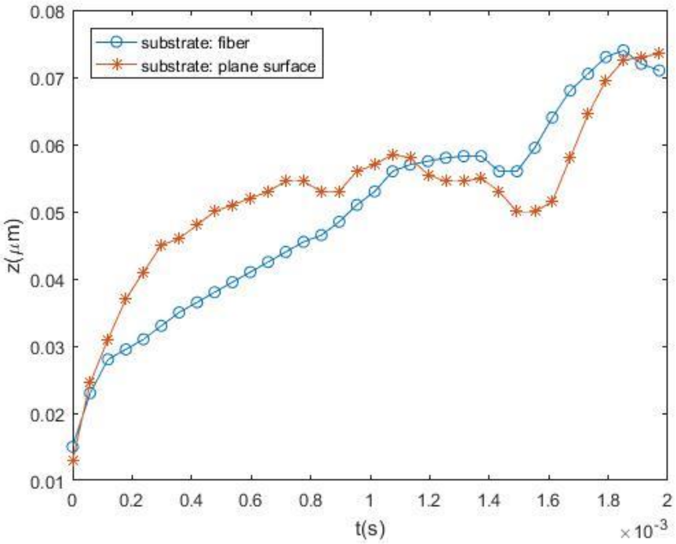

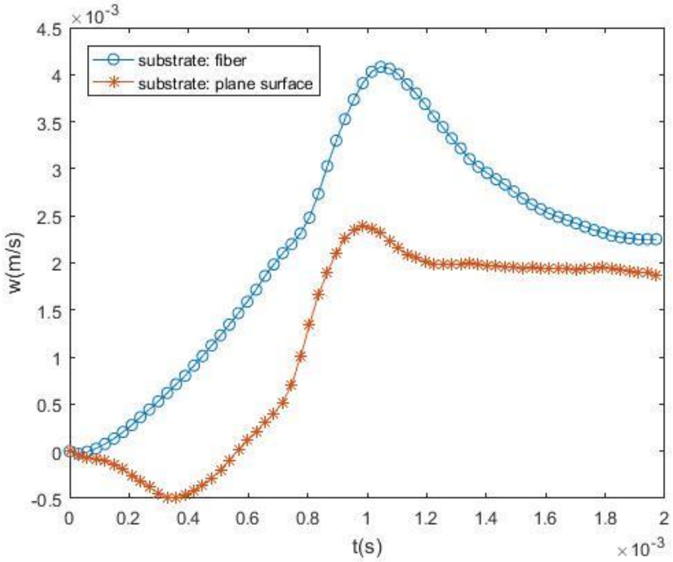

Figure 47 Comparison of the jumping height (top) and the jumping speed (bottom) of the coalesced droplets on two different substrate, fiber and plane surface.

To understand the effect of fiber during the coalescence process and the subsequent jumping phenomenon, the case of coalescence on fiber is being compared to the case of coalescence on a flat substrate. Numerical investigation shows that posterior to the detachment, the droplet jumping off the fiber has a higher jumping height compared to that of the jumping height off the flat surface. Considering the temporal analysis of the events, even though the moment of detachment in the fiber case (t=1.79ms) is quite later than the flat surface(t=1.11ms), once the detachment takes place, the change in height in z-direction is quite large for the droplet with fiber substrate than that of the flat surface. Similarly, as shown in Figure 47, it is evident that there is greater jumping speed in case of the fiber substrate compared to that of the flat surface.

6.2 Substrate Effect

6.2.1 Wedge Curvature (CA=180°)

To study the effect of curvature on the jumping behavior during droplets coalescence, a wedge is placed on the flat surface. In the plots, time is nondimensionalized by the characteristic time $\tau_j = \sqrt{\rho_l r_0^3 / \sigma}$, velocity by capillary-inertia velocity, u_{ci}, momentum by $\rho_l (\frac{8}{3}\pi r_0^3) u_{ci}$ and energy by $\rho_l (\frac{8}{3}\pi r_0^3) u_{ci}^2$. The curvature of the wedge is varied but the other droplet properties are maintained. Our simulations reveal that with an increase in curvature, the jumping capability of the coalesced droplets also increases proportionally.

In all the simulations, the radii of the droplets are set to 380 µm and the properties of liquid and air at 100˚C shown in Table 2 are used. The contact angle to the surface is 180˚, and therefore the surface adhesion does not exist during the simulation. The validation in chapter 3 is considered as the comparison case and the curvature of the wedge is $\kappa = 0$. The beginning status of droplet coalescence on different wedges is shown in Figure 48.

The droplet coalesces in the y-direction and the self-propelled behavior happens in the z-direction. The wedge varies along y-direction and is uniformly shaped along the x-direction. In Figure 48(a), Figure 48(b), and Figure 48(c), the y-axis radii of the wedge are $0.2r_0$, $0.4r_0$ and r_0, respectively. And the curvatures are $\kappa = 5/r_0$, $\kappa = 5/(2r_0)$ and $\kappa = 1/r_0$.

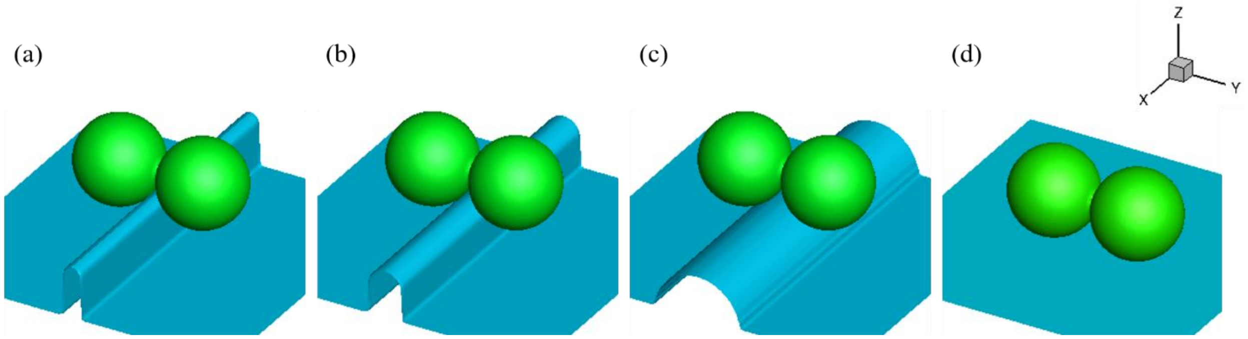

Figure 48 Computational domains of substrate surfaces with different curvatures: (a) $\kappa = 5/r_0$; (b) $\kappa = 5/(2r_0)$; (c) $\kappa = 1/r_0$; (d) $\kappa = 0$ (Flat surface).

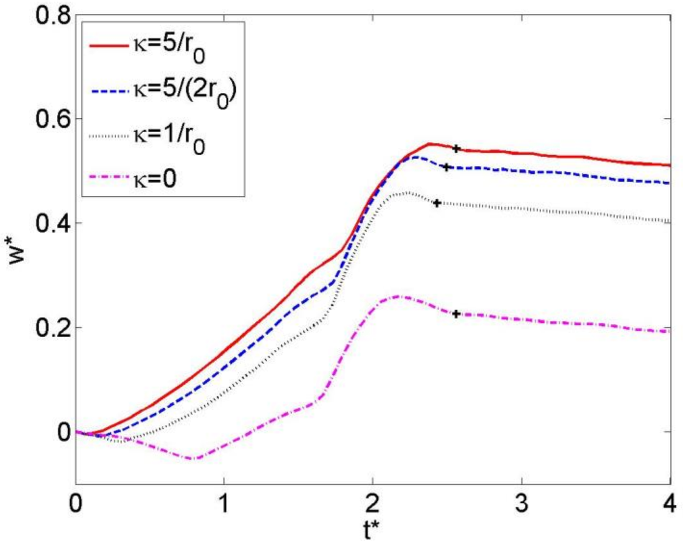

Figure 49 Comparison of z-axis velocity on different curvature surface during droplet jumping process

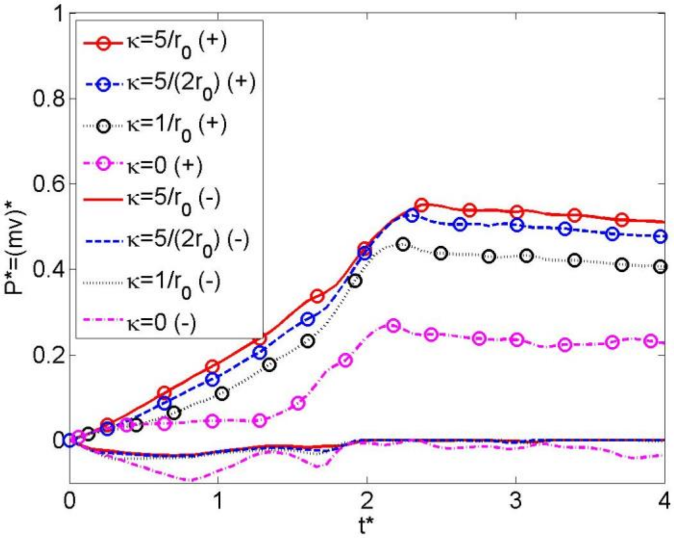

Figure 50 Comparison of z-axis momentums on the surfaces with different curvatures during droplet jumping process

The z-axis velocity of the four cases during the coalescence processes are plotted in Figure 49. The black crosses mark the moment of droplet detachment. Overall, the cases with the wedges have higher z-axis velocities than the case with the flat surface. The jumping speed at the moment of detachment increases with the increase in curvature. The droplet on the wedge with larger curvature accelerates earlier in positive z-axis direction and the acceleration ends later with larger curvature. The droplet detaching-time instant of $\kappa = 1/r_0$ is earlier than the case on the flat surface. However, in the case with wedge, the detaching-time instant is delayed with larger curvature.

In Figure 50 we compare the positive and negative z-axis momentums of the cases. The momentum in positive z-axis direction is higher and has a longer time increment with larger curvature. The magnitude of the momentum in negative z-direction on the wedge is less than the case on the flat surface.

To investigate the differences of z-axis velocity in the cases, the shapes of coalesced droplets are plotted from the views of y-z plane in Figure 51. We compared the shape of the merged drop at different instances: (1) formed liquid bridge contacts the wedge (t*=CT); (2) t*=1.35; (3) t*=1.7; (4) t*=2.0; and (5) droplet reaches the maximum z-axis velocity (t*=MAX); and droplet detaches from substrate (t*=DETACH). Larger curvature leads to earlier contact moment which stops the development of negative momentum and results in an earlier acceleration in the positive z-axis direction. We also plot three other time instances before droplet detachment: t*=1.35, t*=1.7 and t*=2.0 in order to show the droplet deformation. At t*=1.35, the mass center is closer to the bottom of the droplet on the surface with larger curvature. At t*=1.7, small peripheries are formed at the bottom of the droplet near the wedge. At t*=2.0, the small peripheries contact the wedges. The curvature of small peripheries increases with the increase of the curvature. According to the definition of the Laplace pressure (Graf et al., 2006), the pressure difference between a gas region and a liquid region is $\Delta p = 2\gamma / R_c$. The periphery of the droplet has higher pressure difference in the case of a larger curvature. The larger curvature also causes a delay in the occurrence of the maximum z-axis speed.

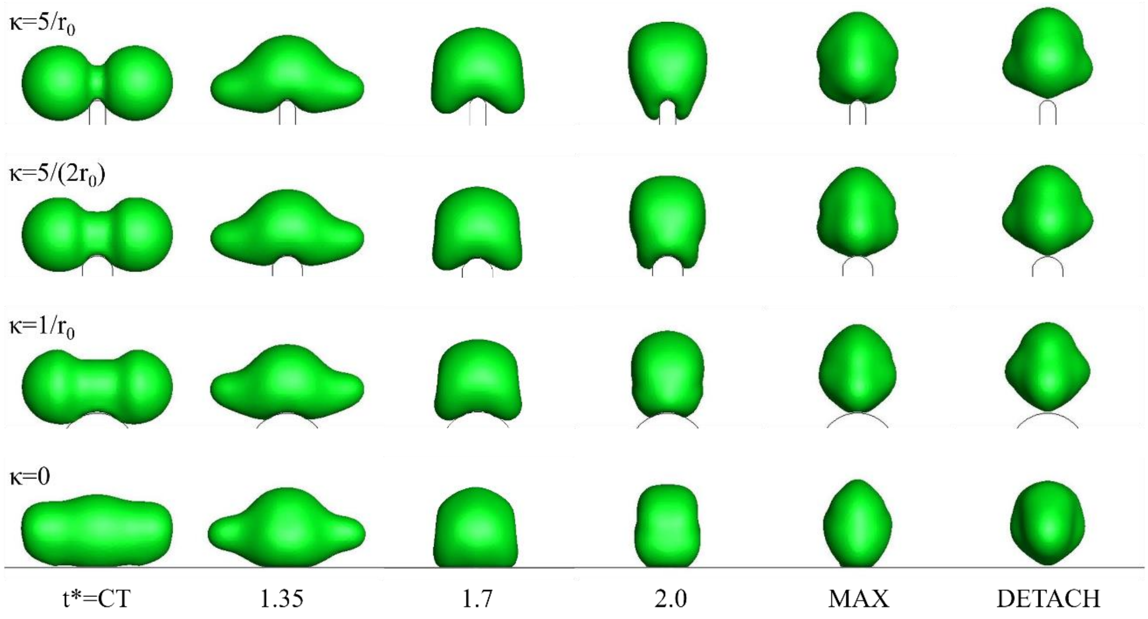

Figure 51 Droplet coalescence process on the surface (θ=180°) with different curvatures (y-z plane)

Here, we also investigate energy transfer during the droplet coalescence. The changes in dimensionless kinetic energy and surface energy are plotted in Figure 52. In Figure 52 (a), we compare the changes in dimensionless total kinetic energy and surface energy of the four cases. At around t*=1.7, ΔE_s^* reaches the minimum value and the case with the flat surface is minimum in the four cases. Due to the presence of the wedge, the small peripheries begin to appear near the wedge, as shown in Figure 51, which causes the surface area on the curved wedge to be larger than the case on the flat surface. The difference immediately disappears at t*=1.9 offset by droplet deformation while the peripheries are kept. From t* = 2.0 to the moment of droplet detachment, the decrement of surface energy in the case of the curved wedge decreases is more than in the case of the flat surface. As observed in Figure 51, the small peripheries on the wedge surface disappear at t* =MAX. The surface energy saved in the peripheries is released and transferred into kinetic energy. The released surface energy and the kinetic energy increases with the curvature. As shown in Figure 52 (a), the increment of kinetic energy on the wedged surface is more than on the flat surface and the magnitude of increment is higher with larger curvature.

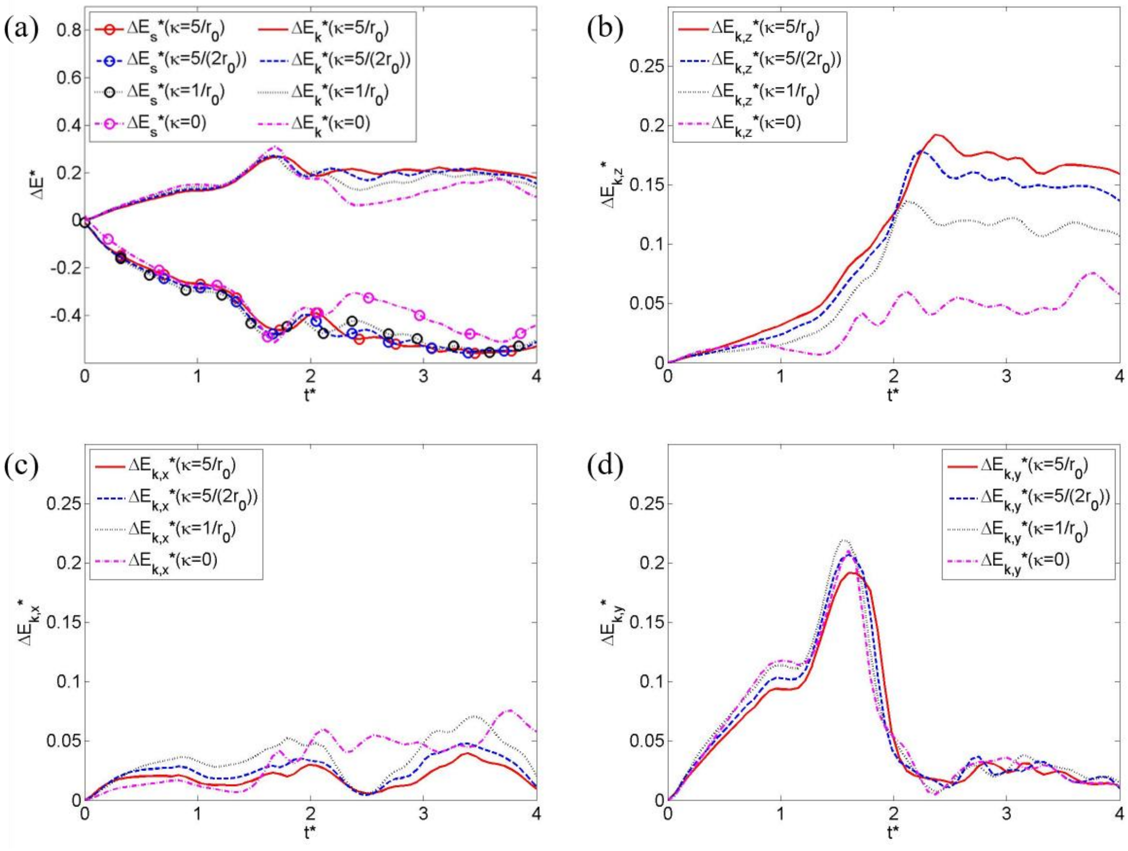

Figure 52 Comparison of dimensionless energy change during the self-propelled process for the cases with $\kappa = 5/r_0$, $\kappa = 5/(2r_0)$, $\kappa = 1/r_0$ and $\kappa = 0$: (a) the changes in kinetic energy and surface energy; (b) the change in kinetic energy in z-axis; (c) the change in kinetic energy in x-axis; (d) the change in kinetic energy in y-axis.

In Figure 52 (b), same as z-axis velocity, $\Delta E_{k,z}$ in the case of flat surface has the lowest increase and the increase in kinetic energy is higher on the wedge with larger curvature. In Figure 52 (c), during droplet detachment, $\Delta E_{k,x}$ on the curved surface is lower than that of the flat surface regardless of wedge curvature. The increase in kinetic energy in the x-axis direction is suppressed by the curved surface. $\Delta E_{k,y}$ has no significant difference between the four cases, as shown in Figure 52 (d).

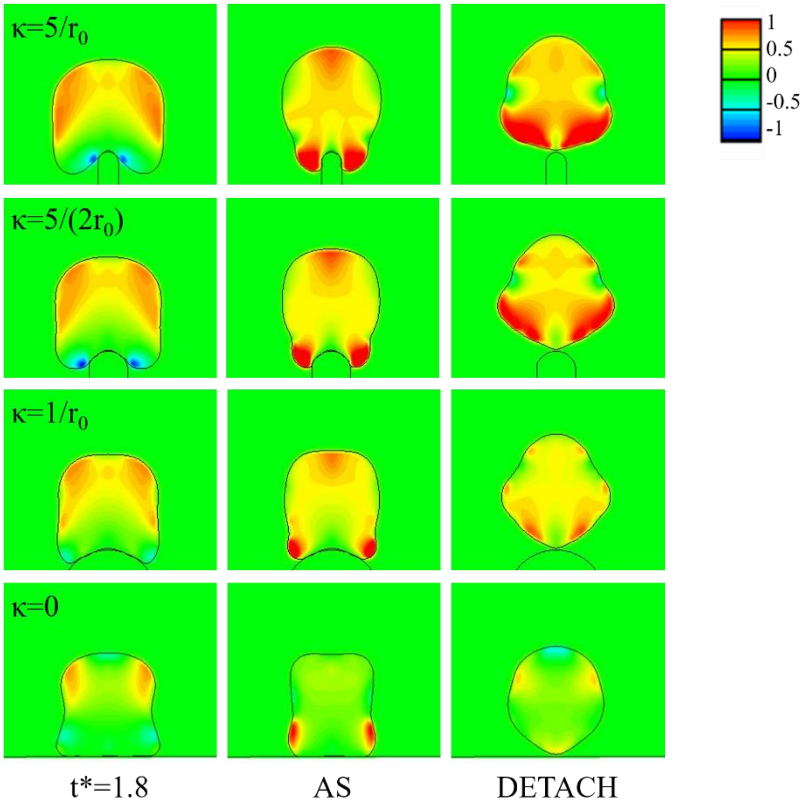

Figure 53 z-axis velocity contours of droplet on the substrate surfaces with different curvatures

To investigate how the jumping motion changes over time, the z-axis velocity contours are plotted on y-z plane at three time instants: 1) t*=1.8, 2) the beginning of acceleration due to the periphery, and 3) moment of droplet detachment. Overall, the case with larger curvature shows more area of positive z-axis velocity in the droplet. At t*=1.8, negative z-axis velocity appears on the contour plot at the bottom of the droplet. At the beginning of acceleration, the positive velocity appears the bottom of the droplet due to the curvature area on the small peripheries causing high pressure difference in the droplet. The droplet starts to accelerate at the bottom and the time instants for the four cases are 2.2, 2.05, 2.0 and 2.0, respectively. The small peripheries need extra time to form. At the instance of droplet detachment, the upward velocity near the wedge is higher when the curvature is larger.

6.2.2 Droplet Size

To validate whether the droplet coalescence on the wedge still obeys the capillary inertial scaling law or not, we compare the coalesced droplets of different sizes (40μm, $100\mu m$ and $380\mu m$) on the same wedge ($\kappa = 5/r_0$). In terms of the dimensionless z-axis velocity, as shown in Figure 54, the three cases have nearly identical results. The case with larger droplet size has larger dimensional time for the same dimensionless time, therefore. And the dimensionless z-axis velocity of $r_0 = 380\mu m$ decrease more rapidly after detachment from the wedge. Therefore, the jumping speed at moment of detachment still obeys capillary-inertial scaling law $w_j \sim r_0^{-1/2}$.

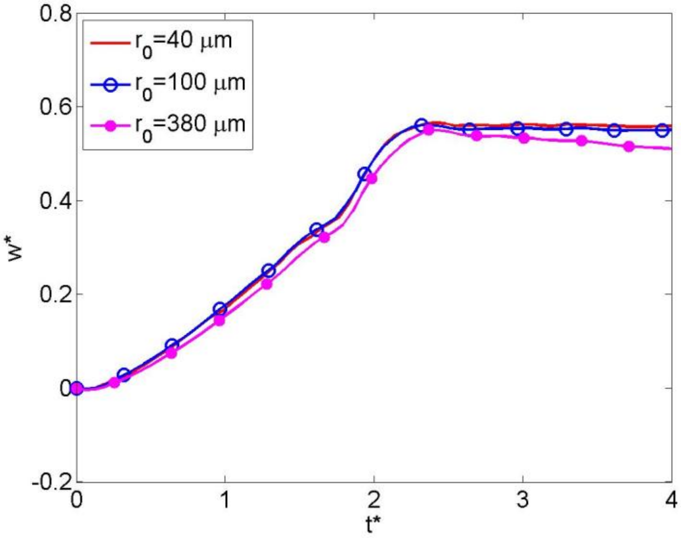

Figure 54 Comparison of dimensionless z-axis velocity with radii of $40\mu\text{m}$, $100\mu m$ and $380\mu m$.

6.2.3 Surface Adhesion on the Wedged Surfaces (κ=5/r0)

To understand the effect surface adhesion, three simulation cases of droplet coalescence are carried out on the surfaces with same curvature (κ=5/r0) but with different contact angles, 90°, 110° and 180°, which represent surface adhesion from strong to weak. Our simulation shows that droplets on the surface with a contact angle of 90° lack of self-propelling capability. The dimensionless z-axis velocity profile is plotted in Figure 55 and shows that the z-axis velocity is affected by surface adhesion during the whole coalescence process. The momentums in the positive and the negative z-axis directions are plotted in Figure 56. The adhesion on the surface can both increase the magnitude of negative z momentum and decrease the magnitude of positive z momentum.

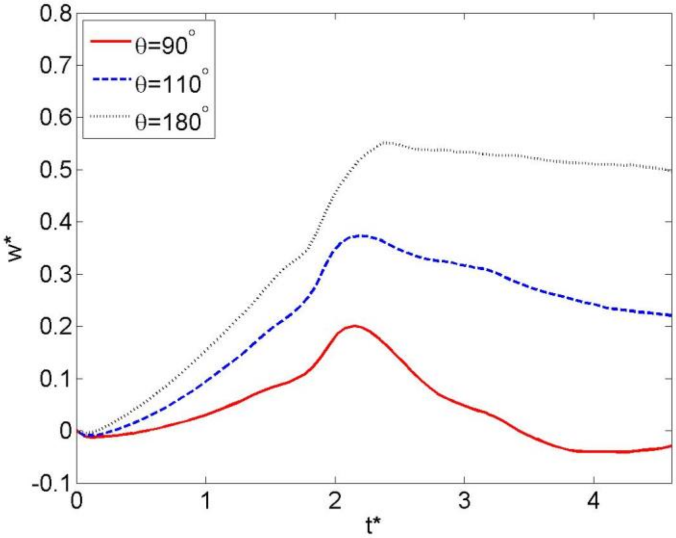

Figure 55 Comparison of z-axis velocity on the surfaces with the same curvature of $\kappa = 5 / r_0$ but different contact angles during droplet jumping process

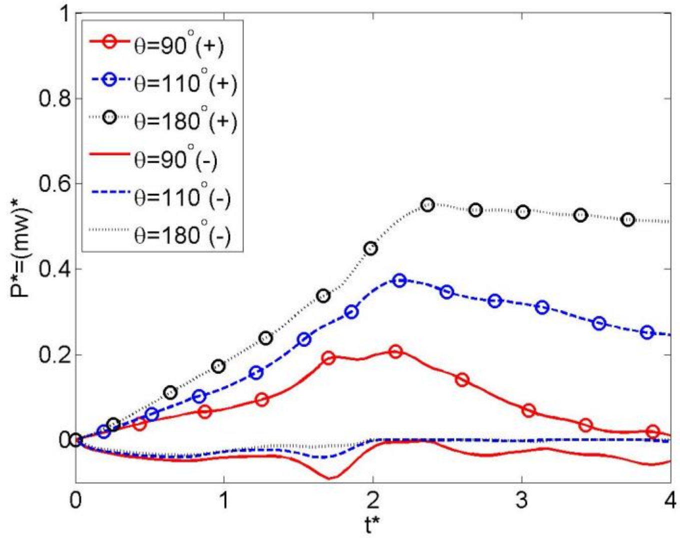

Figure 56 Comparison of positive and negative z-axis momentums on the surfaces with the same curvature of $\kappa = 5 / r_0$ but different contact angles during droplet jumping process

The contour plots of the z-axis velocity for different contact angles are plotted in Figure 57. At t* = 1.35, the droplet shapes are different, and the droplet has more contact area with the wedge on surface with strong adhesion for the droplet is easy to attach to the substrate surface. At t* = 1.8, significant negative velocity appears in the bottom of the droplet. The negative velocity is more obvious for the surface with strong adhesion. At t* = 2.18, when the droplet starts to accelerate by the peripheries, the acceleration is most significant in the case with θ=180°. The detaching moment of θ=110° and θ=180° is at t* = 4.07 and t* = 2.56, respectively. The detaching velocity much higher on the surface of θ=180°. The droplet of θ=90° is unable to detach from the substrate.

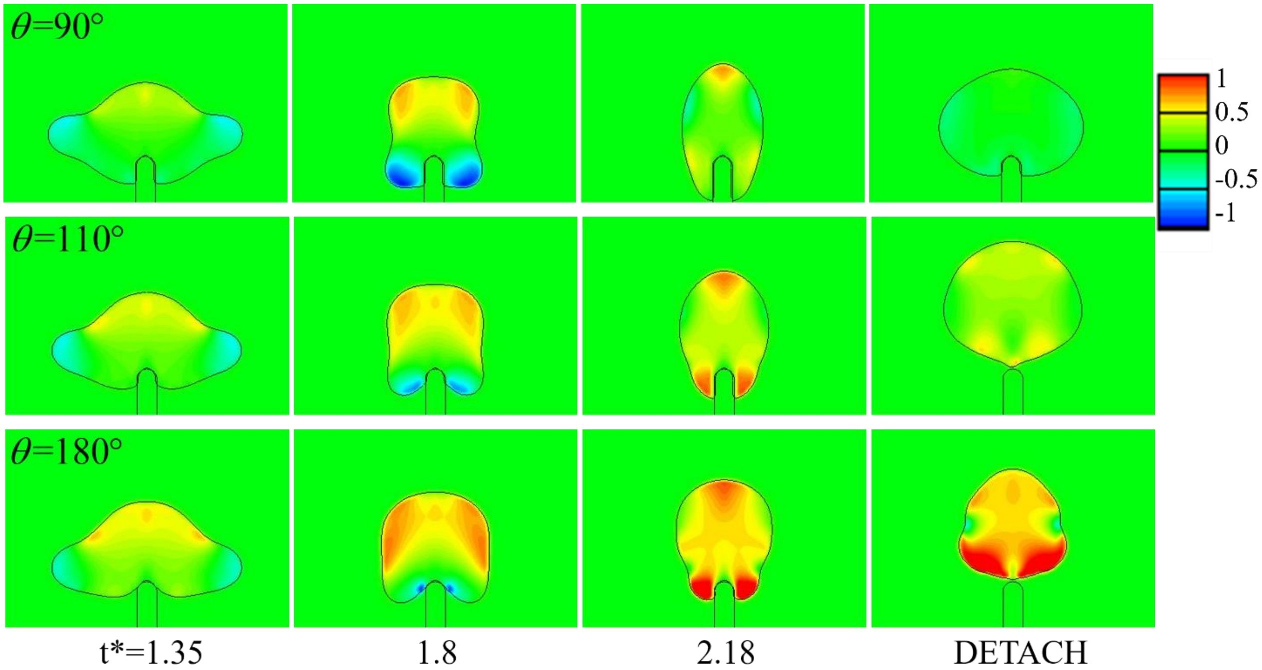

Figure 57 Dimensionless z-axis velocity contours on the surfaces with the same curvature of $\kappa = 5/r_0$ but different contact angles

CHAPTER 7. CONCLUSIONS

In the present study, the droplet coalescence on a non-wetting flat surfaces and wedged surfaces was numerically investigated. An approximate projection method was used to solve the Navier-Stokes equations, and the moment-of-fluid method was used to reconstruct the interfaces. The numerical results showed that the moment-of-fluid method accurately captured the interfaces of the deforming droplet. The numerical method was validated with published experimental results and good agreement was achieved.

The jumping velocity, vertical momentum and energy history were analyzed to investigate the jumping mechanism. The substrate prevented the downward motion of the droplet in liquid bridge formation and the elongation of droplet oscillation. During the droplet detachment, the substrate prevented the droplet elongation in the vertical direction and kept the droplet with smaller surface area, therefore, more energy was reserved as kinetic energy, especially in the positive z-direction. The substrate interfering the oscillation of merged droplet leads to the jumping behavior of coalesced droplet. The jumping velocity obeys the capillary-inertial scaling law.

The jumping velocity is also affected by the relative approaching speed between the two droplets. Increasing the relative speed made the coalescence an inertia dominated motion. The kinetic energy existing at the beginning of the coalescence were transferred into surface energy. The surface energy releasing was not observed in high speed cases.

The curvature of the substrate surface has positive effects on the droplet jumping velocity. On the wedged surface, the droplets contacted the substrate earlier preventing the development of negative jumping velocity at an earlier stage. The coalesced droplets formed small peripheries near the curved wedge, and the peripheries were smoothed out in the later stage releasing surface energy to accelerate the droplet in the jumping direction. The jumping velocity increased with increasing of substrate curvature. The jumping velocity still obeys the capillary-inertial scaling law on the curved wedge. The surface adhesion decreased the jumping velocity and even prevented the jumping behavior.

REFERENCE

Ahn, H.T., & Shashkov, M. (2007). Multi-material interface reconstruction on generalized polyhedral meshes. *Journal of Computational Physics*, *226*, 2096-2132

Ahn, H.T., & Shashkov, M. (2009). Adaptive moment-of-fluid method. *Journal of Computational Physics, 228*, 2792-2821

Ashgriz, N., & Poo, J. (1990). Coalescence and separation in binary collisions of liquid drops. *Journal of Fluid Mechanics, 221*, 183-204

Baroudi, L., Nagel, S.R., Morris, J.F., & Lee, T. (2015). Dynamics of viscous coalescing droplets in a saturated vapor phase. *Physics of Fluids, 27*, 121702

Becker, E., Hiller, W., & Kowalewski, T. (1991). Experimental and theoretical investigation of large-amplitude oscillations of liquid droplets. *Journal of Fluid Mechanics, 231*, 189-210

Bernardin, J., & Mudawar, I. (1999). The Leidenfrost point: experimental study and assessment of existing models. *Transactions-American Society of Mechanical Engineers Journal of Heat Transfer, 121*, 894-903

Bhushan, B., & Jung, Y.C. (2011). Natural and biomimetic artificial surfaces for superhydrophobicity, self-cleaning, low adhesion, and drag reduction. *Progress in Materials Science, 56*, 1-108

Boreyko, J.B., & Chen, C.-H. (2009). Self-propelled dropwise condensate on superhydrophobic surfaces. *Physical Review Letters, 103*, 184501

Boreyko, J.B., & Chen, C.-H. (2013a). Vapor chambers with jumping-drop liquid return from superhydrophobic condensers. *International Journal of Heat and Mass Transfer, 61*, 409-418

Boreyko, J.B., & Collier, C.P. (2013b). Delayed frost growth on jumping-drop superhydrophobic surfaces. *ACS nano, 7*, 1618-1627

Boreyko, J.B., Hansen, R.R., Murphy, K.R., Nath, S., Retterer, S.T., & Collier, C.P. (2016). Controlling condensation and frost growth with chemical micropatterns. *Scientific reports, 6*

Burton, Z., & Bhushan, B. (2005). Hydrophobicity, adhesion, and friction properties of nanopatterned polymers and scale dependence for micro-and nanoelectromechanical systems. *Nano letters, 5*, 1607-1613

Butt, H.-J., Graf, K., & Kappl, M. (2006). *Physics and chemistry of interfaces*. John Wiley & Sons

Chandrasekhar, S. (2013). *Hydrodynamic and hydromagnetic stability*. Courier Corporation

Cheng, Y., Xu, J., & Sui, Y. (2016). Numerical investigation of coalescence-induced droplet jumping on superhydrophobic surfaces for efficient dropwise condensation heat transfer. *International Journal of Heat and Mass Transfer, 95,* 506-516

Chorin, A.J. (1968). Numerical solution of the Navier-Stokes equations. *Mathematics of computation, 22,* 745-762

Chorin, A.J. (1969). On the convergence of discrete approximations to the Navier-Stokes equations. *Mathematics of computation, 23,* 341-353

De Gennes, P.-G. (1985). Wetting: statics and dynamics. *Reviews of modern physics, 57,* 827

De Gennes, P.-G., Brochard-Wyart, F., & Quéré, D. (2013). *Capillarity and wetting phenomena: drops, bubbles, pearls, waves*. Springer Science & Business Media

De Ruiter, J., Lagraauw, R., Van Den Ende, D., & Mugele, F. (2015). Wettability-independent bouncing on flat surfaces mediated by thin air films. *Nature physics, 11,* 48

Dietz, C., Rykaczewski, K., Fedorov, A., & Joshi, Y. (2010). Visualization of droplet departure on a superhydrophobic surface and implications to heat transfer enhancement during dropwise condensation. *Applied Physics Letters, 97,* 033104

Dyadechko, V., & Shashkov, M. (2005). Moment-of-fluid interface reconstruction. *Los Alamos report LA-UR-05-7571*

Dyadechko, V., & Shashkov, M. (2008). Reconstruction of multi-material interfaces from moment data. *Journal of Computational Physics, 227,* 5361-5384

Eggers, J., Lister, J.R., & Stone, H.A. (1999). Coalescence of liquid drops. *Journal of Fluid Mechanics, 401,* 293-310

Enright, R., Miljkovic, N., Dou, N., Nam, Y., & Wang, E.N. (2013). Condensation on superhydrophobic copper oxide nanostructures. *Journal of Heat Transfer, 135,* 091304

Enright, R., Miljkovic, N., Sprittles, J., Nolan, K., Mitchell, R., & Wang, E.N. (2014). How coalescing droplets jump. *ACS nano, 8,* 10352-10362

Eral, H., & Oh, J. (2013). Contact angle hysteresis: a review of fundamentals and applications. *Colloid and polymer science, 291*, 247-260

Gao, L., & McCarthy, T.J. (2006). The “lotus effect” explained: two reasons why two length scales of topography are important. *Langmuir, 22,* 2966-2967

Giacomello, A., Chinappi, M., Meloni, S., & Casciola, C.M. (2012). Metastable wetting on superhydrophobic surfaces: continuum and atomistic views of the Cassie-Baxter–Wenzel transition. *Physical Review Letters, 109,* 226102

Gottfried, B., Lee, C., & Bell, K. (1966). The Leidenfrost phenomenon: film boiling of liquid droplets on a flat plate. *International Journal of Heat and Mass Transfer, 9,* 1167-1188

Graf, K., & Kappl, M. (2006). *Physics and chemistry of interfaces*. John Wiley & Sons

Hao, C., Li, J., Liu, Y., Zhou, X., Liu, Y., Liu, R., Che, L., Zhou, W., Sun, D., & Li, L. (2015). Superhydrophobic-like tunable droplet bouncing on slippery liquid interfaces. *Nature communications, 6*

Hoffman, R.L. (1975). A study of the advancing interface. I. Interface shape in liquid—gas systems. *Journal of Colloid and Interface Science, 50*, 228-241

Janssens, S.D., Koizumi, S., & Fried, E. (2017). Behavior of self-propelled acetone droplets in a Leidenfrost state on liquid substrates. *Physics of Fluids, 29,* 032103

Jemison, M. (2014). An asymptotically preserving method for multiphase flow. In: The Florida State University

Jemison, M., Loch, E., Sussman, M., Shashkov, M., Arienti, M., Ohta, M., & Wang, Y. (2013a). A coupled level set-moment of fluid method for incompressible two-phase flows. *Journal of Scientific Computing,* 1-38

Jemison, M., Loch, E., Sussman, M., Shashkov, M., Arienti, M., Ohta, M., & Wang, Y. (2013b). A coupled level set-moment of fluid method for incompressible two-phase flows. *Journal of Scientific Computing, 54,* 454-491

Jemison, M., Sussman, M., & Arienti, M. (2014). Compressible, multiphase semi-implicit method with moment of fluid interface representation. *Journal of Computational Physics, 279*, 182-217

Jiang, T.-S., Soo-Gun, O., & Slattery, J.C. (1979). Correlation for dynamic contact angle. *Journal of Colloid and Interface Science, 69,* 74-77

Kang, M., Fedkiw, R.P., & Liu, X.-D. (2000). A boundary condition capturing method for multiphase incompressible flow. *Journal of Scientific Computing, 15*, 323-360

Kim, H., Yang, S., Rao, S.R., Narayanan, S., Kapustin, E.A., Furukawa, H., Umans, A.S., Yaghi, O.M., & Wang, E.N. (2017). Water harvesting from air with metal-organic frameworks powered by natural sunlight. *Science, 356*, 430-434

Koch, K., Bhushan, B., Jung, Y.C., & Barthlott, W. (2009). Fabrication of artificial Lotus leaves and significance of hierarchical structure for superhydrophobicity and low adhesion. *Soft Matter, 5*, 1386-1393

Kolinski, J.M., Mahadevan, L., & Rubinstein, S. (2014). Drops can bounce from perfectly hydrophilic surfaces. *EPL (Europhysics Letters), 108*, 24001

Kwatra, N., Su, J., Grétarsson, J.T., & Fedkiw, R. (2009). A method for avoiding the acoustic time step restriction in compressible flow. *Journal of Computational Physics, 228*, 4146-4161

Ladyzhenskaya, O.A., & Silverman, R.A. (1969). *The mathematical theory of viscous incompressible flow*. Gordon & Breach New York

Lam, C., Wu, R., Li, D., Hair, M., & Neumann, A. (2002). Study of the advancing and receding contact angles: liquid sorption as a cause of contact angle hysteresis. *Advances in colloid and interface science, 96*, 169-191

Lautrup, B. (2011). *Physics of continuous matter: exotic and everyday phenomena in the macroscopic world*. CRC press

Lee, A., Moon, M.-W., Lim, H., Kim, W.-D., & Kim, H.-Y. (2012). Water harvest via dewing. *Langmuir, 28*, 10183-10191

Leidenfrost, J.G. (1756). *De aquae communis nonnullis qualitatibus tractatus*. Ovenius

Li, G., Lian, Y., Guo, Y., Jemison, M., Sussman, M., Helms, T., & Arienti, M. (2015). Incompressible multiphase flow and encapsulation simulations using the moment ‐ of ‐ fluid method. *International Journal for Numerical Methods in Fluids, 79*, 456-490

Lienhard, J.H. (2013). *A heat transfer textbook*. Courier Corporation

Linder, N. (2015). Numerical Simulation of Complex Wetting. In: Technische Universität

Liu, F., Ghigliotti, G., Feng, J.J., & Chen, C.-H. (2014a). Numerical simulations of self-propelled jumping upon drop coalescence on non-wetting surfaces. *Journal of Fluid Mechanics, 752*, 39-65

Liu, F., Ghigliotti, G., Feng, J.J., & Chen, C.-H. (2014b). Self-propelled jumping upon drop coalescence on Leidenfrost surfaces. *Journal of Fluid Mechanics, 752*, 22-38

Liu, Y., Andrew, M., Li, J., Yeomans, J.M., & Wang, Z. (2015). Symmetry breaking in drop bouncing on curved surfaces. *Nature communications, 6*

Liu, Y., Moevius, L., Xu, X., Qian, T., Yeomans, J.M., & Wang, Z. (2014c). Pancake bouncing on superhydrophobic surfaces. *Nature physics, 10*, 515

Lv, C., Hao, P., Yao, Z., Song, Y., Zhang, X., & He, F. (2013). Condensation and jumping relay of droplets on lotus leaf. *Applied Physics Letters, 103*, 021601

McNaught, A.D., & McNaught, A.D. (1997). *Compendium of chemical terminology*. Blackwell Science Oxford

Miljkovic, N., Enright, R., Nam, Y., Lopez, K., Dou, N., Sack, J., & Wang, E.N. (2012a). Jumping-droplet-enhanced condensation on scalable superhydrophobic nanostructured surfaces. *Nano letters, 13*, 179-187

Miljkovic, N., Enright, R., & Wang, E.N. (2012b). Effect of droplet morphology on growth dynamics and heat transfer during condensation on superhydrophobic nanostructured surfaces. *ACS nano, 6*, 1776-1785

Nam, Y., Kim, H., & Shin, S. (2013). Energy and hydrodynamic analyses of coalescence-induced jumping droplets. *Applied Physics Letters, 103*, 161601

Neumann, A.W., & Kwok, D. (1998). Contact angles and surface energetics. *Horizons 2000–aspects of colloid and interface science at the turn of the millenium* (pp. 170-184): Springer

Orme, M. (1997). Experiments on droplet collisions, bounce, coalescence and disruption. *Progress in Energy and Combustion Science, 23*, 65-79

Peng, B., Wang, S., Lan, Z., Xu, W., Wen, R., & Ma, X. (2013). Analysis of droplet jumping phenomenon with lattice Boltzmann simulation of droplet coalescence. *Applied Physics Letters, 102*, 151601

Qian, J., & Law, C. (1997). Regimes of coalescence and separation in droplet collision. *Journal of Fluid Mechanics, 331*, 59-80

Quéré, D. (2013). Leidenfrost dynamics. *Annual Review of Fluid Mechanics, 45*, 197-215

Rayleigh, L. (1879a). On the capillary phenomena of jets. In, *Proc. R. Soc. London* (pp. 71-97)

Rayleigh, L. (1879b). On the capillary phenomena of jets. *Proc. R. Soc. London, 29*, 71-97

Reay, D., McGlen, R., & Kew, P. (2013). *Heat pipes: theory, design and applications*. Butterworth-Heinemann

Richard, D., Clanet, C., & Quéré, D. (2002). Surface phenomena: Contact time of a bouncing drop. *Nature, 417*, 811-811

Rose, J. (2002). Dropwise condensation theory and experiment: a review. *Proceedings of the Institution of Mechanical Engineers, Part A: Journal of Power and Energy, 216*, 115-128

Rose, J., & Glicksman, L. (1973). Dropwise condensation—the distribution of drop sizes. *International Journal of Heat and Mass Transfer, 16*, 411-425

Shah, P., Fan, L., Kao, I., & Erickson, L. (1972). Modeling of growth processes with two liquid phases: a review of drop phenomena, mixing, and growth. *Advances in Applied Microbiology, 15*, 367-414

Shi, Y., Tang, G., & Xia, H. (2015). Investigation of coalescence-induced droplet jumping on superhydrophobic surfaces and liquid condensate adhesion on slit and plain fins. *International Journal of Heat and Mass Transfer, 88*, 445-455

Sprittles, J., & Shikhmurzaev, Y. (2012). Coalescence of liquid drops: Different models versus experiment. *Physics of Fluids, 24*, 122105

Strang, G. (1968). On the construction and comparison of difference schemes. *SIAM Journal on Numerical Analysis, 5*, 506-517

Sussman, M., Almgren, A.S., Bell, J.B., Colella, P., Howell, L.H., & Welcome, M.L. (1999). An adaptive level set approach for incompressible two-phase flows. *Journal of Computational Physics, 148*, 81-124

Temam, R. (1969). Sur l'approximation de la solution des équations de Navier-Stokes par la méthode des pas fractionnaires (II). *Archive for Rational Mechanics and Analysis, 33*, 377-385

Torresin, D., Tiwari, M.K., Del Col, D., & Poulikakos, D. (2013). Flow condensation on copper-based nanotextured superhydrophobic surfaces. *Langmuir, 29*, 840-848

Wang, F.-C., Yang, F., & Zhao, Y.-P. (2011). Size effect on the coalescence-induced self-propelled droplet. *Applied Physics Letters, 98*, 053112

Wang, Q., Yao, X., Liu, H., Quéré, D., & Jiang, L. (2015). Self-removal of condensed water on the legs of water striders. *Proceedings of the National Academy of Sciences, 112*, 9247-9252

Wang, Y., Simakhina, S., & Sussman, M. (2012). A hybrid level set-volume constraint method for incompressible two-phase flow. *Journal of Computational Physics, 231*, 6438-6471

Washburn, E.W. (1921). The dynamics of capillary flow. *Physical review, 17*, 273

Wu, D., Wu, S.Z., Chen, Q.D., Zhang, Y.L., Yao, J., Yao, X., Niu, L.G., Wang, J.N., Jiang, L., & Sun, H.B. (2011). Curvature - Driven Reversible In Situ Switching Between Pinned and Roll - Down Superhydrophobic States for Water Droplet Transportation. *Advanced Materials, 23*, 545-549

Yokoi, K., Vadillo, D., Hinch, J., & Hutchings, I. (2009). Numerical studies of the influence of the dynamic contact angle on a droplet impacting on a dry surface. *Physics of Fluids, 21*, 072102

Young, T. (1805). An essay on the cohesion of fluids. *Philosophical Transactions of the Royal Society of London, 95*, 65-87

Yuan, Y., & Lee, T.R. (2013). Contact angle and wetting properties. *Surface science techniques* (pp. 3-34): Springer

Zhang, K., Liu, F., Williams, A.J., Qu, X., Feng, J.J., & Chen, C.-H. (2015). Self-propelled droplet removal from hydrophobic fiber-based coalescers. *Physical Review Letters, 115*, 074502

Zhang, Q., He, M., Chen, J., Wang, J., Song, Y., & Jiang, L. (2013). Anti-icing surfaces based on enhanced self-propelled jumping of condensed water microdroplets. *Chemical Communications, 49*, 4516-4518

Zhang, Q., He, M., Zeng, X., Li, K., Cui, D., Chen, J., Wang, J., Song, Y., & Jiang, L. (2012). Condensation mode determines the freezing of condensed water on solid surfaces. *Soft Matter, 8*, 8285-8288

Zou, J., Wang, P.F., Zhang, T.R., Fu, X., & Ruan, X. (2011). Experimental study of a drop bouncing on a liquid surface. *Physics of Fluids, 23*, 044101

CURRICULUM VITAE

Yan Chen
Department of Mechanical Engineering,
University of Louisville, Louisville, KY 40292
yan.chen@louisville.edu

Education

- Ph.D. Mechanical Engineering 2018
University of Louisville, Louisville, KY

- M.S. Mechanical Engineer 2011
University of Louisville, Louisville, KY

- B.S. Water Supply and Sewage Engineering 2009
North China University of Water Conservancy and Electric Power, Henan, China

Journal Publications

Y. Chen, Y. Lian, "Numerical Investigation of Coalescence-induced Self-propelled Behavior of Droplets on the Curved surfaces", Manuscript in preparation, 2018.

Y. Chen, Y. Lian, "Numerical Investigation of Coalescence-induced Self-propelled Behavior of Droplets on non-wetting surfaces", Phys. Fluids, 2018.

Y. Chen, Y. Lian, "Numerical Investigation of Vortex Dynamics in an H-Rotor Vertical Axis Wind Turbine", Engineering Applications of Computational Fluid Mechanics (2015): 1-12.

Conference Publications

- **Y. Chen**, K. Hord, R Prater, L. Bai, and Y. Lian, "Design Optimization of a Vertical Axis Wind Turbine Using a Genetic Algorithm and Surrogate Models," AIAA Paper 2012-5434, 2012